

PENNSSTATE



IGNITION AND COMBUSTION CHARACTERISTICS OF  
METALLIZED PROPELLANTS

Final Report - Phase I (June 1989 - December 1992)  
NASA Lewis Research Center  
Grant No. NAG 3-1004

S. R. Turns, Principal Investigator  
D. C. Mueller

Department of Mechanical Engineering  
and  
Propulsion Engineering Research Center  
The Pennsylvania State University  
University Park, PA 16802

January 1993

N93-19412

Unclas

G3/28 0148102

(NASA-CR-192285) IGNITION AND  
COMBUSTION CHARACTERISTICS OF  
METALLIZED PROPELLANTS Final  
Report, Jun. 1989 - Dec. 1992  
(Pennsylvania State Univ.) 56 p

1

2

3

4

5

6

7

8

9

10

11

12

13

14

15

16

17

18

19

20

IGNITION AND COMBUSTION CHARACTERISTICS OF  
METALLIZED PROPELLANTS

Final Report - Phase I  
(June 1989 - December 1992)

S. R. Turns, Principal Investigator  
and  
D. C. Mueller

Department of Mechanical Engineering  
and  
Propulsion Engineering Research Center  
The Pennsylvania State University  
University Park, PA 16802

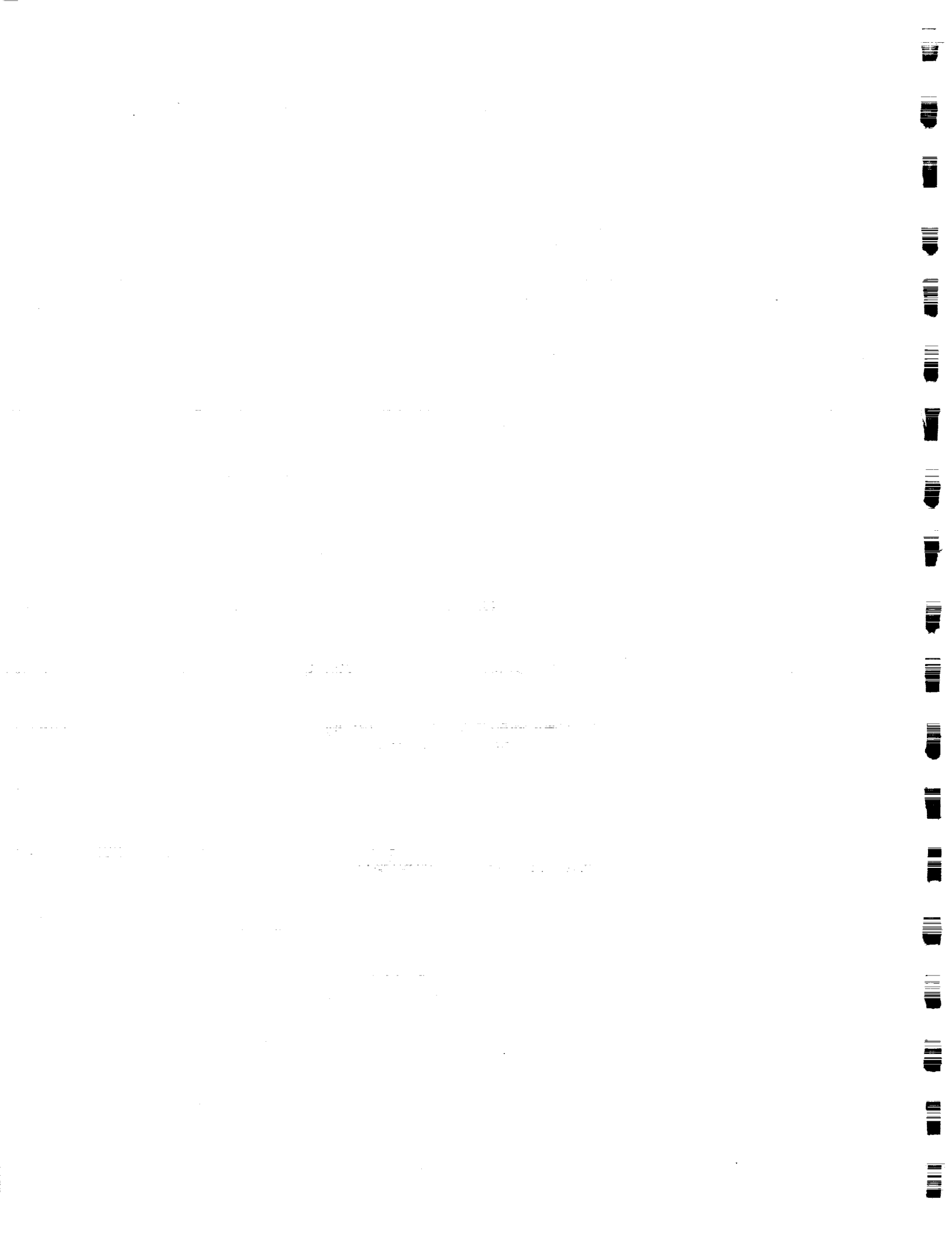
for

NASA Lewis Research Center

Grant No. NAG 3-1004

Bryan Palaszewski  
NASA Technical Officer

January 1993



## SUMMARY

Experimental and analytical investigations focusing on secondary atomization and ignition characteristics of aluminum/liquid hydrocarbon slurry propellants were conducted. Experimental efforts included the application of a laser-based, two-color, forward-scatter technique to simultaneously measure, free-flying slurry droplet diameters and velocities for droplet diameters in the range of 10-200  $\mu\text{m}$ . A multi-diffusion flame burner was used to create a high-temperature environment into which a dilute stream of slurry droplets could be introduced. Narrowband measurements of radiant emission were used to determine if ignition of the aluminum in the slurry droplet had occurred. Models of slurry droplet shell formation were applied to aluminum/liquid hydrocarbon propellants and used to ascertain the effects of solids loading and ultimate particle size on the minimum droplet diameter that will permit secondary atomization. For a 60 weight-percent Al slurry, the limiting critical diameter was predicted to be 34.7  $\mu\text{m}$ , which is somewhat greater than the 20-25  $\mu\text{m}$  limiting diameters determined in the experiments. A previously developed model of aluminum ignition in a slurry droplet was applied to the present experiments and found to predict ignition times in reasonable agreement with experimental measurements. A model was also developed that predicts the mechanical stress in the droplet shell and a parametric study was conducted. A one-dimensional model of a slurry-fueled rocket combustion chamber was developed. This model includes the processes of liquid hydrocarbon burnout, secondary atomization, aluminum ignition, and aluminum combustion. Also included is a model for radiant heat transfer from the hot aluminum oxide particles to the chamber walls. Exercising this model shows that only a modest amount of secondary atomization is required to reduce residence times for aluminum burnout, and thereby, maintain relatively short chamber lengths. The model also predicts radiant heat transfer losses to the walls to be only approximately 3 percent of the fuel energy supplied. Additional work is required to determine the effects of secondary atomization on two-phase losses in the nozzle.

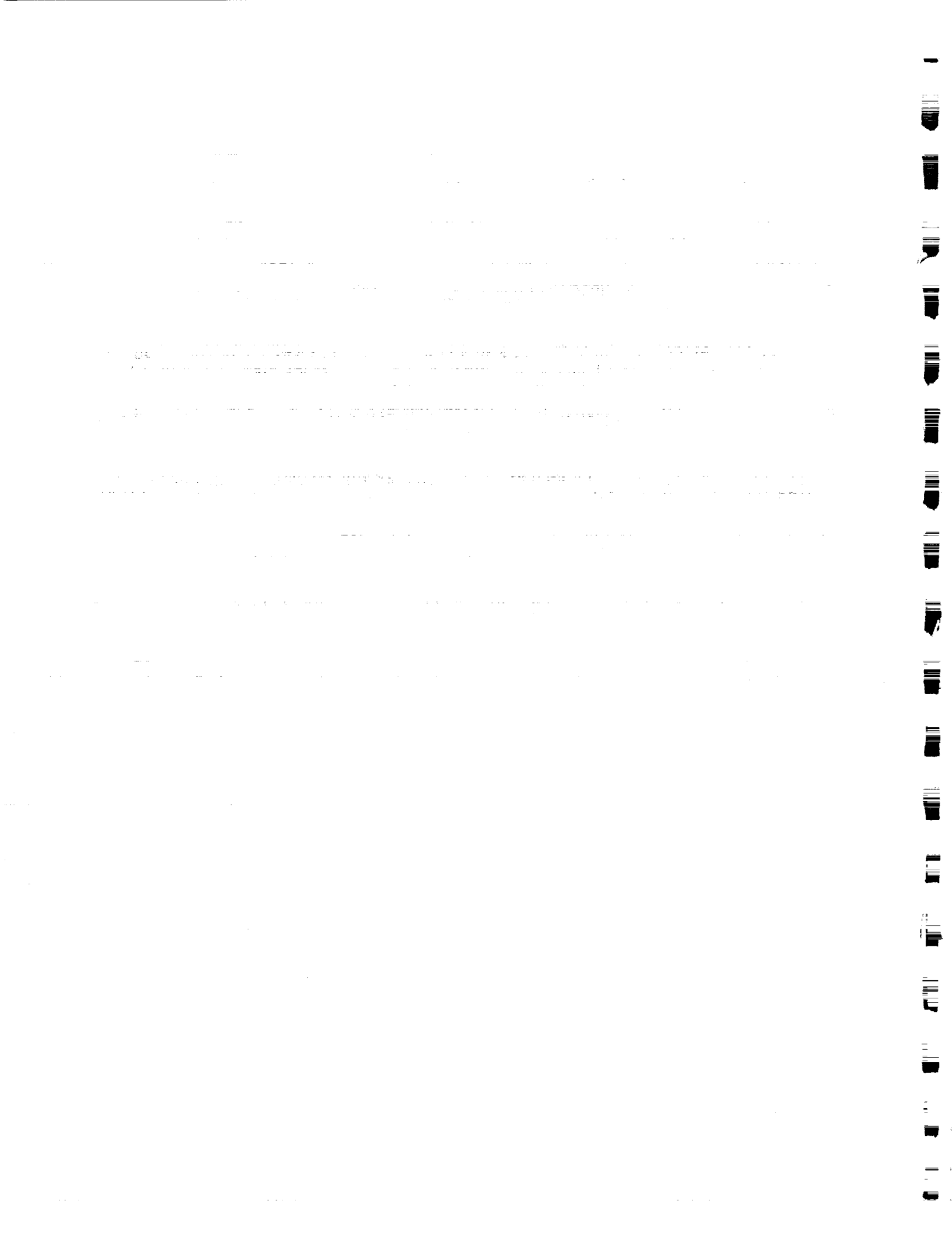


# TABLE OF CONTENTS

	<u>Page</u>
SUMMARY.....	i
TABLE OF CONTENTS.....	ii
LIST OF FIGURES .....	iii
NOMENCLATURE.....	v
INTRODUCTION .....	1
PROGRAM OBJECTIVES .....	2
PROGRAM ACCOMPLISHMENTS .....	2
Experimental Systems .....	2
Particle Size and Velocity Measurements .....	2
Aluminum Combustion Detection .....	4
Burner and Atomization Systems .....	4
Slurry Droplet Disruption Models .....	4
Overview .....	6
Limiting Drop Size for Shell Formation.....	6
Disruption Model .....	11
Model Results.....	15
Limiting Drop Size for Disruption - Theory and Experiment.....	15
One-Dimensional Combustion Chamber Model Development .....	23
Overview .....	23
Model Description.....	24
Mass Conservation .....	24
Energy Conservation.....	26
Radiation Heat Transfer .....	28
Momentum Conservation .....	30
Slurry Combustion.....	31
Solution Method .....	33
One-Dimensional Model Results.....	33
TABLE 1 .....	33
SUMMARY AND CONCLUSIONS.....	37
ACKNOWLEDGMENTS .....	42
REFERENCES .....	42
APPENDIX - PUBLICATIONS AND PRESENTATIONS .....	47





## LIST OF FIGURES

- Figure 1. Schematic of experimental diagnostics for droplet size and velocity measurements and aluminum combustion detection.
- Figure 2. Schematic diagram of burner and spray generator.
- Figure 3. Schematic of critical shell formation, shell growth, vapor-void formation, and shell sealing.
- Figure 4. Dimensionless limiting initial diameter for the formation of a rigid shell as a function of aluminum mass fraction.
- Figure 5. Shell diameter, fraction of total particles forming a critical shell, and the total number of particles versus initial droplet diameter.
- Figure 6. 50 wt% aluminum slurry droplet ( $d_o = 50 \mu\text{m}$ ) shell stress, liquid fuel mass fraction, and shell thickness as functions of time, assuming various shell sealing time intervals ( $d_{ult} = 5 \mu\text{m}$ ).
- Figure 7. 50 wt% aluminum slurry droplet ( $d_o = 200 \mu\text{m}$ ) shell stress, liquid fuel mass fraction, and shell thickness as functions of time, assuming various shell sealing time intervals ( $d_{ult} = 5 \mu\text{m}$ ).
- Figure 8. 60 wt% aluminum slurry particle size distribution 5 mm above the burner with no flame present.
- Figure 9. 60 wt% aluminum slurry particle size distribution 5 mm above the burner with flame present.
- Figure 10. 60 wt% aluminum slurry particle size distribution 10 mm above the burner with flame present.
- Figure 11. 60 wt% aluminum slurry particle size distribution 15 mm above the burner with flame present.
- Figure 12. Normalized droplet size distribution used in combustor code.
- Figure 13. Gas and droplet velocities versus axial location for a 60 wt% Al slurry assuming no secondary atomization.
- Figure 14. Gas and droplet velocities versus axial location for a 60 wt% Al slurry assuming a secondary atomization fragmentation ratio of 40.
- Figure 15. Mass fraction of major gas species and gas temperature versus axial location. Data is for a 60 wt% Al slurry assuming a secondary atomization fragmentation ratio of 5.

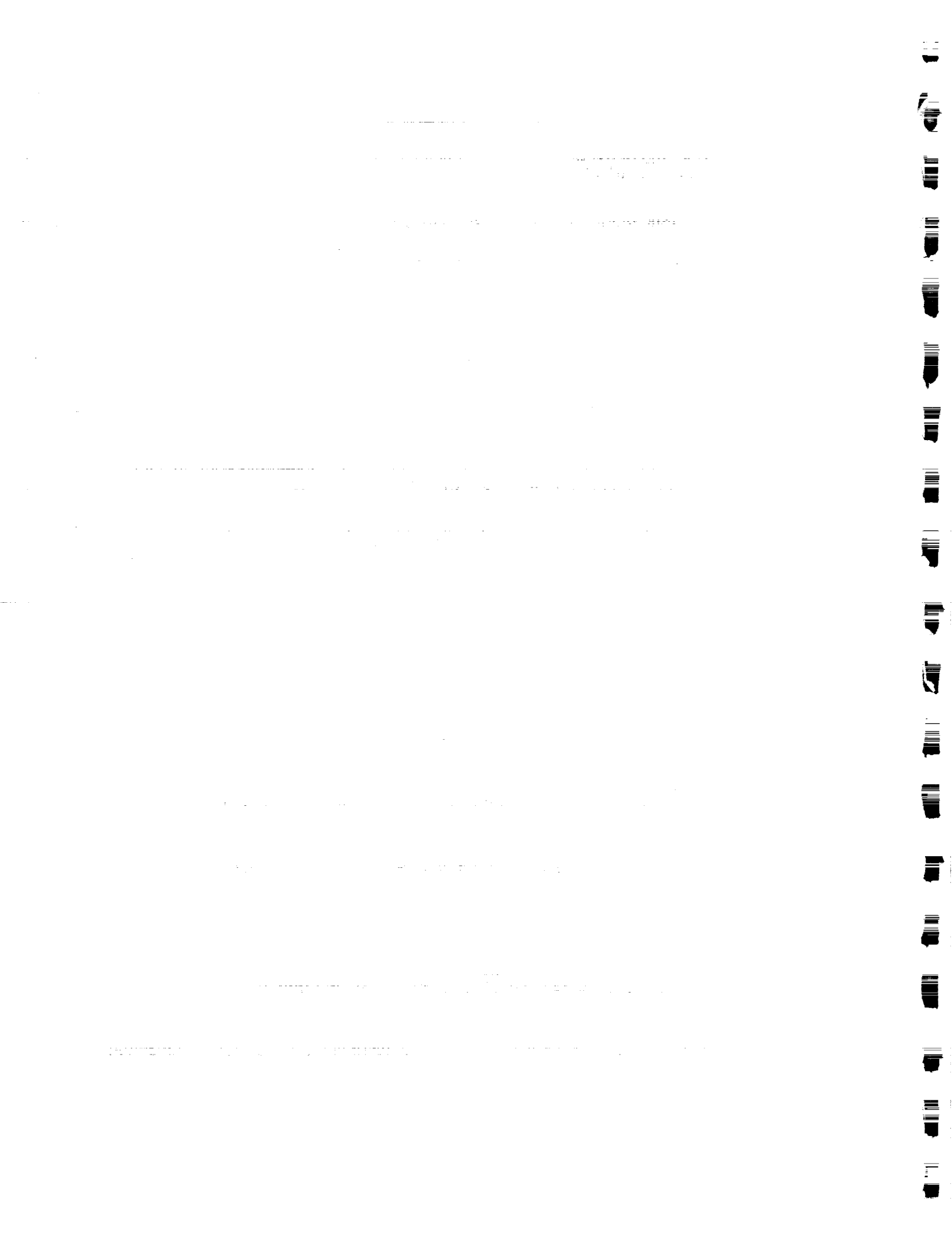


Figure 16. Chamber burnout distance as a function of secondary atomization fragmentation ratio for a 60 wt% Al slurry.

Figure 17. Final oxide agglomerate diameter as a function of secondary atomization fragmentation ratio. Data is for a 60 wt% Al slurry.



## NOMENCLATURE

$a$ -	absorption coefficient
$\bar{a}$ -	droplet acceleration
$A_p$ -	droplet surface area
$c, c_p$ -	specific heat
$C_a$ -	absorption cross-section
$C_s$ -	scattering cross-section
$C_D$ -	drag coefficient
$d$ -	diameter
$d_p$ -	shell interior equivalent diameter
$d_v$ -	vapor void equivalent diameter
$F_\lambda(T)$ -	fraction of total radiation emitted by a blackbody at temperature $T$ in the wavelength interval between 0 and $\lambda$
$\bar{F}$ -	force acting on a droplet
$h$ -	specific enthalpy
$h_{fv}$ -	specific heat of vaporization
$\bar{h}$ -	average convective heat transfer coefficient
$I_b$ -	blackbody radiant intensity
$I_0, I_1$ -	modified Bessel functions
$j$ -	droplet size class
$k$ -	conductivity
$K_D$ -	optical thickness
$M$ -	mass or number of droplet size classes in the combustion chamber
$\dot{m}$ -	mass flux of evaporating fuel or mass flux through the combustion chamber
$n$ -	dimensionless shell thickness ( $n=\delta/d_u$ ) or wavelength interval
$N$ -	number density of $Al_2O_3$ fume particles
$N_p$ -	number of particles
$\bar{N}_j$ -	fraction of total droplets in given size class, $j$
$N/\tau$ -	number of droplets passing through combustor control volume per unit time
$P$ -	pressure
$q_r$ -	radiation heat flux from solid combustion products to chamber wall
$q_c$ -	convective heat flux
$R$ -	combustion chamber radius



Re-	Reynolds number
s-	characteristic radiation path length
r-	mean shell radius or slurry droplet radius
t-	time
$t_c$ -	time at which rigid shell forms
$t_d$ -	time at which droplet disrupts
$t_s$ -	time at which rigid shell becomes impermeable
T-	temperature
u-	specific internal energy
$u_{fv}$ -	specific internal energy of vaporization
$u_g$ -	gas velocity
$u_p$ -	droplet velocity
U-	total system internal energy
v-	specific volume
V-	volume
x-	mixture quality, defined as the vapor mass fraction in the mixture or axial location in the combustion chamber
$Y_s$ -	solids mass fraction
z-	compressibility factor

#### Greek

$\beta$ -	fragmentation ratio (number of secondary droplets/initial droplet)
$\delta$ -	shell thickness
$\eta$ -	fraction of Al droplet mass that forms as $Al_2O_3$ on droplet surface
$\lambda$ -	wavelength
$\rho$ -	density
$\sigma$ -	shell stress
$\sigma_s$ -	scattering coefficient
$\theta$ -	volume fraction
$\Omega_o$ -	scattering albedo

#### Subscripts

Al-	aluminum
$Al_2O_3$ -	aluminum oxide agglomerate
b-	boiling
c-	critical





d-	droplet
f-	liquid hydrocarbon, Al flame, or $\text{Al}_2\text{O}_3$ fume particles
g-	ambient gas or gas flow in the combustion chamber
j-	droplet size class
LH-	liquid hydrocarbon
lim-	minimum limit
m-	liquid-vapor mixture or melting
o-	initial or known
p-	shell
s-	solids
v-	vapor
w-	chamber wall
$\infty$ -	ambient



## INTRODUCTION

Slurry or gelled propellants in which a solid constituent is suspended in a combustible liquid have been of interest for propulsion applications for several decades. Depending upon the application, these propellants are advantageous because of either their energy content per unit mass or per unit volume. Many solid chemical elements are attractive for formulating slurry or gelled propellants. For example, carbon, aluminum, and boron all offer substantial increases in volumetric heat of combustion compared to hydrocarbon fuels, while on a gravimetric basis, only boron provides an increased heating value [1]. For rocket applications, specific impulse and mass density control payload capability for a fixed vehicle configuration. Thus, high mass density propellant systems such as  $O_2/Al/RP-1$  become attractive possible alternatives to more conventional propellant systems. Recent fuel performance and mission studies [2-6] have shown that aluminum-based slurry propellants can offer significant potential benefits over non-metallized propellants. For example, use of aluminum with  $O_2/H_2$  propellants has the potential for increasing the payload delivered to Mars from low earth orbit (LEO) by over 20 percent [3]. The addition of aluminum to nitrogen tetroxide/monomethyl hydrazine (NTO/MMH) propellants may also enable planetary missions that would otherwise not be possible with neat NTO/MMH [5]. It has also been shown that using aluminum can reduce combustion instabilities in liquid hydrocarbon propellants [7-8].

Several key technical issues impact the use of  $Al/RP-1$  slurries or gels in propulsion systems. Among these are rheological properties and ignition and combustion characteristics. In the area of rheology, questions concerning the proper formulation to provide a stable, easily pumpable slurry with acceptable spray characteristics remain unanswered. Recent studies of propellant formulation [9-11] and spray characteristics [12] have made inroads in understanding how to deal with the conflicting requirements of long-term storability without separation of the solid and liquid phases yet maintaining sufficiently low viscosities so that the slurries are easily pumped and sprayed.

Various laboratory-scale experiments have demonstrated combustion of aluminum slurry fuels in both rocket thrust chambers [7,8,13,14] and air-breathing combustors [15-17]. In all but one of these studies [17], successful ignition and stable combustion were achieved. In some cases, combustion efficiencies were as high as 99 percent. In order to achieve high combustion and thrust efficiencies, the aluminum must ignite and burn in the residence time available, and the two-phase losses associated with the condensed-phase products must be minimized. Both of these requirements are facilitated by having small slurry droplets, since prior work [18,19] has shown that the individual aluminum particles in the slurry droplets can form agglomerates that ultimately burn as a single aluminum droplet. Good atomization of slurry fuels, however, can be difficult to achieve. Fortunately, the additives used to produce desirable rheological properties can lead to secondary atomization of large slurry droplets, as observed in studies of single droplets of  $Al/JP-10$  [11,20,21] and other slurries [22-24]. In particular, the surfactants used as wetting and dispersing agents promote the breakup of burning slurry droplets into a very large number of smaller droplets. The aluminum in these small secondary droplets readily ignites and burns. In addition, the particle sizes of the aluminum oxide products are smaller, potentially decreasing two-phase flow losses.

The focus of the present investigation is this secondary atomization process. This report highlights the major objectives and accomplishments of our research. More detailed information can be found in previous reports and publications [25-31].

## **PROGRAM OBJECTIVES**

The overall objective of research is the development of a fundamental understanding of the ignition and combustion of aluminum-based slurry (or gel) propellant droplets using a combination of experiment and analysis. Primary specific technical objectives include the following:

1. Understanding the roles of aluminum particle size, surfactants, and gellants (or other additives) in promoting or inhibiting secondary atomization of propellant droplets;
2. The extension of previously developed analytical models to address various important phenomena associated with secondary atomization that were neglected in the simplest model;
3. Development of a simple one-dimensional model of a slurry-fueled rocket engine that incorporates secondary atomization, carrier fuel burnout, and aluminum ignition and combustion. This model will allow the evaluation of secondary atomization effects on combustion efficiency and two-phase flow losses.

## **PROGRAM ACCOMPLISHMENTS**

### **Experimental Systems**

Apparatus and experimental techniques were developed to study the secondary atomization of slurry droplets in the 10-100  $\mu\text{m}$  diameter size range. Specifically, non-intrusive optical methods were implemented to measure droplet size and velocity, and to detect aluminum combustion of free-flying droplets in a high-temperature environment.

Particle Size and Velocity Measurements - Slurry droplet and/or agglomerates and product particle size and velocity measurements are accomplished using a single-particle sizing system based on a two-color forward scattering technique [32]. A schematic of the system is shown in Fig. 1. Particle sizing is performed by correlating particle diameter with the intensity of near-forward scattering from a particle passing through the center of an Ar-ion beam. Right-angle scattering from a He-Ne laser beam, coaxially focused inside the Ar-ion beam is used to trigger data acquisition, thus, assuring that the particle passed through the center of the Ar-ion beam. A 50/50 beam splitter, incorporated in the right-angle collection optics, separates the 90° scattered light signal into two components. The first component triggers the data acquisition, while the second is used for aluminum combustion detection, as described below. Particle size versus output signal calibration [27] were performed using various diameter pinholes

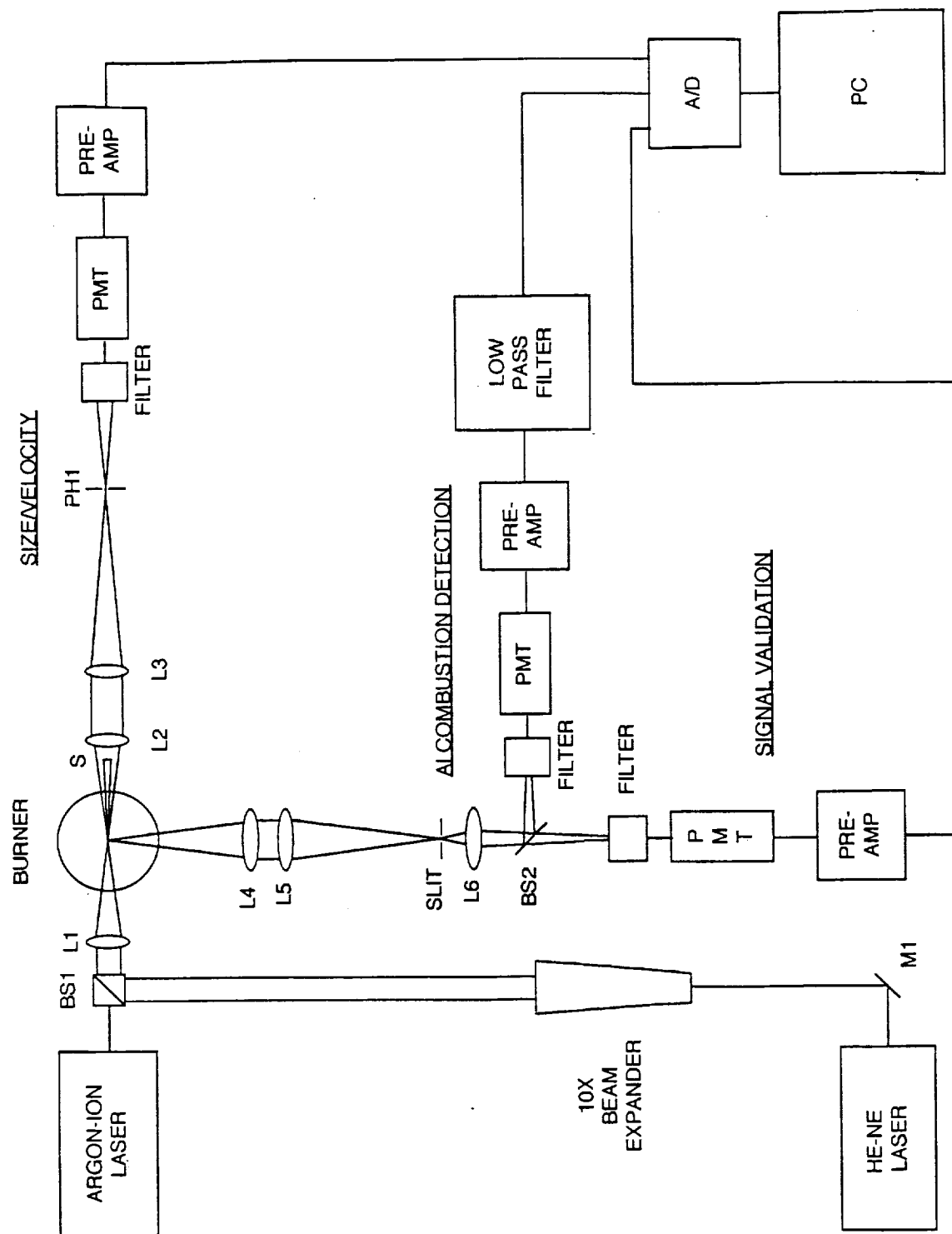


FIGURE 1. Schematic of experimental diagnostics for droplet size and velocity measurements and aluminum combustion detection.

(10-100 mm) and were found to agree with Mie theory. These calibrations were also verified using monodisperse water droplets, the diameters of which were measured using video images [27]. Detailed discussion of the particle size and velocity measurement system is provided in Refs. [25-27].

**Aluminum Combustion Detection** - An aluminum combustion detection system, consisting of a 395 nm bandpass filter, a photomultiplier tube (PMT), and a 10 kHz low-pass electronic filter, is incorporated in the 90° scatter optics to detect spectral line emissions from vapor-phase aluminum [33,34]. Since vapor-phase aluminum only exists during aluminum combustion, these spectral emissions provide a valid indication of aluminum combustion.

Because broadband emission from molten aluminum,  $\text{Al}_2\text{O}_3$ , and burning hydrocarbons produces a low-level background signal on the combustion detection channel, a minimum threshold signal level is used to discriminate between valid aluminum combustion and this background radiation. From comparisons of combustion channel voltages for burning JP-10 droplets and 60 wt% aluminum slurry droplets, a 2 volt threshold was chosen as the criterion for aluminum combustion since this was the highest signal level observed for the JP-10 droplets. Additional details of the system development and calibration are presented in Ref. [28].

**Burner and Atomization Systems** - A non-premixed burner produces a homogeneous post-flame region that approximates that of a premixed flat-flame burner with none of the inherent flashback problems [35, 36]. A schematic of the burner system developed is shown in Fig. 2. Slurry is fed to a gas-type atomizer (Spraying Systems 1/8J) by a syringe pump. Slurry droplets generated in a spray chamber at the bottom of the burner pass through a tube located along the burner centerline, and emerge at the center of the burner face. Adjusting the relative composition of the  $\text{N}_2/\text{CH}_4$  atomizing gas mixture permits matching of the central tube and flame stoichiometries. Approximately three percent of the atomizing flow is carried through the central tube, while the remainder of the flow is vented. A valve on the vent line controls the pressure differential between the chamber and the surroundings, permitting a matching of gas exit velocities between the central tube and the burner flames. More detailed information concerning the burner and spraying systems and experience in dealing with very high viscosity slurries is found in Refs. [25-27].

## **Slurry Droplet Disruption Models**

Analytic models of the processes leading up to droplet disruption were developed and applied to aluminum-based slurries. These models included shell formation and internal pressure build-up, of which the latter is a major advance in understanding secondary atomization of slurries. The models for rigid shell formation, slurry droplet ignition, and aluminum burnout were exercised and compared with experimental results for droplets with initial sizes ranging from 10-80  $\mu\text{m}$ . A major issue addressed in this part of the research is the role of size of the aluminum particles that constitute the slurry. Since the size of the aluminum powder used in slurry fuels is of the order of several microns [10,11], and since the formation of a dense surface layer of particles is one mechanism for droplet disruption [21-24,37], the question arises of whether or not secondary atomization occurs when the parent droplet contains relatively few aluminum

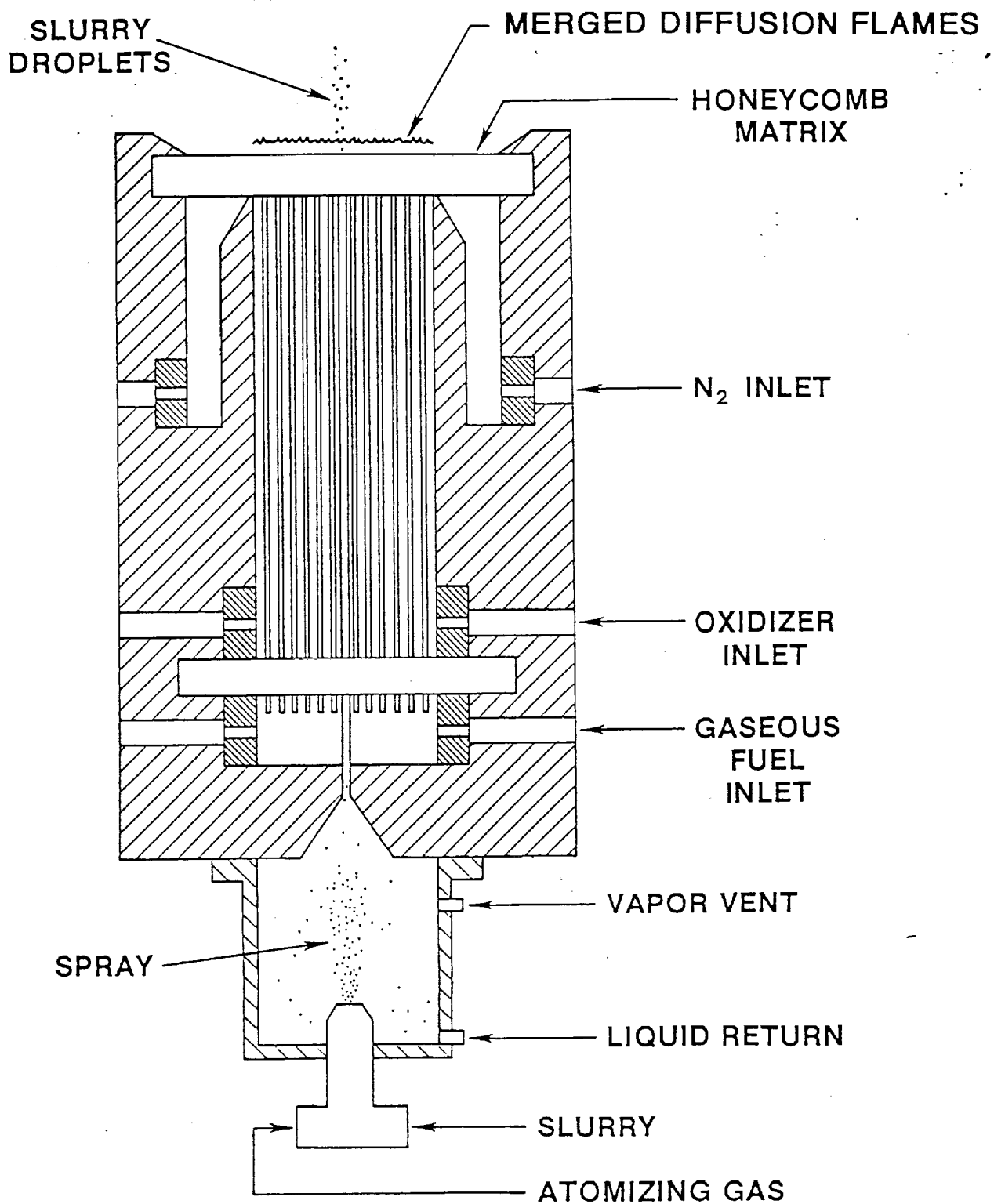


FIGURE 2. Schematic diagram of burner and spray generator.

particles, rather than thousands. In previous work [20], we studied relatively large droplets (200-1200  $\mu\text{m}$ ), while in the present investigation, our focus is the secondary atomization of much smaller aluminum slurry droplets (20-100  $\mu\text{m}$ ).

Overview - Recent studies [22,24,37] present a simple theoretical framework for shell formation, an event which is considered to be an essential precursor to secondary atomization. This framework is schematically illustrated in Fig. 3. When a slurry droplet is exposed to a hot ambient environment, heat transfer from the gas flow causes liquid to vaporize and the droplet surface to regress. As liquid vaporizes at the droplet surface, the aluminum particles that were suspended in the vaporized liquid remain behind at the droplet surface, causing the number density of aluminum particles at the droplet surface to increase.

If the initial droplet is large enough and there is a sufficient number of aluminum particles in the droplet, the particle number density will increase until a rigid shell is formed by particles coming into contact with each other. Experimental evidence suggests that rigidity occurs when the particle surface layer is nominally three particle diameters thick with a solids volume fraction approximately equal to a cubic packing ( $\theta_{s,p} = 0.524$ ) [22,24]. With the rigid shell, further liquid vaporization occurs at a constant external diameter. Additional growth of the shell thickness occurs, and mass conservation requires that a vapor-void form somewhere in the droplet interior (Fig. 3c). Some time interval after rigid shell formation, surfactant pyrolysis makes the shell impermeable and liquid vaporization ceases (Fig. 3d) [24,37]. Heat transfer to the droplet continues, causing droplet internal pressure and rigid shell stresses to rise until the shell fails.

Limiting Drop Size for Shell Formation - Rigid shell formation requires that there are enough solid particles initially present in a slurry drop to form a hollow sphere with a specified thickness. The total number of particles in a droplet with an initially uniform solids volume fraction is [22]

$$N_{p,\text{tot}} = \theta_{s,o} (d_o / d_u)^3 . \quad (1)$$

The number of particles in the shell is a function of the assumed shell thickness and the droplet diameter when the shell becomes rigid and is expressed as [22]

$$N_{p,s} = \theta_{s,p} \left[ d_s^3 - (d_s - 2nd_u)^3 \right] / d_u^3 . \quad (2)$$

The remainder of the particles are in the liquid slurry core, which has the same solids volume fraction as the initial state, i.e., [22]

$$N_{p,\text{tot}} - N_{p,s} = \theta_{s,o} \pi (d_s - 2nd_u)^3 / 6 . \quad (3)$$

The size of the droplet after enough liquid has evaporated to form the rigid shell can be obtained by substituting Eqs. (1) and (2) into Eq. (3) and solving for  $d_s$ . This involves a cubic equation that is easily solved numerically using Newton's method.



## SHELL FORMATION STAGES

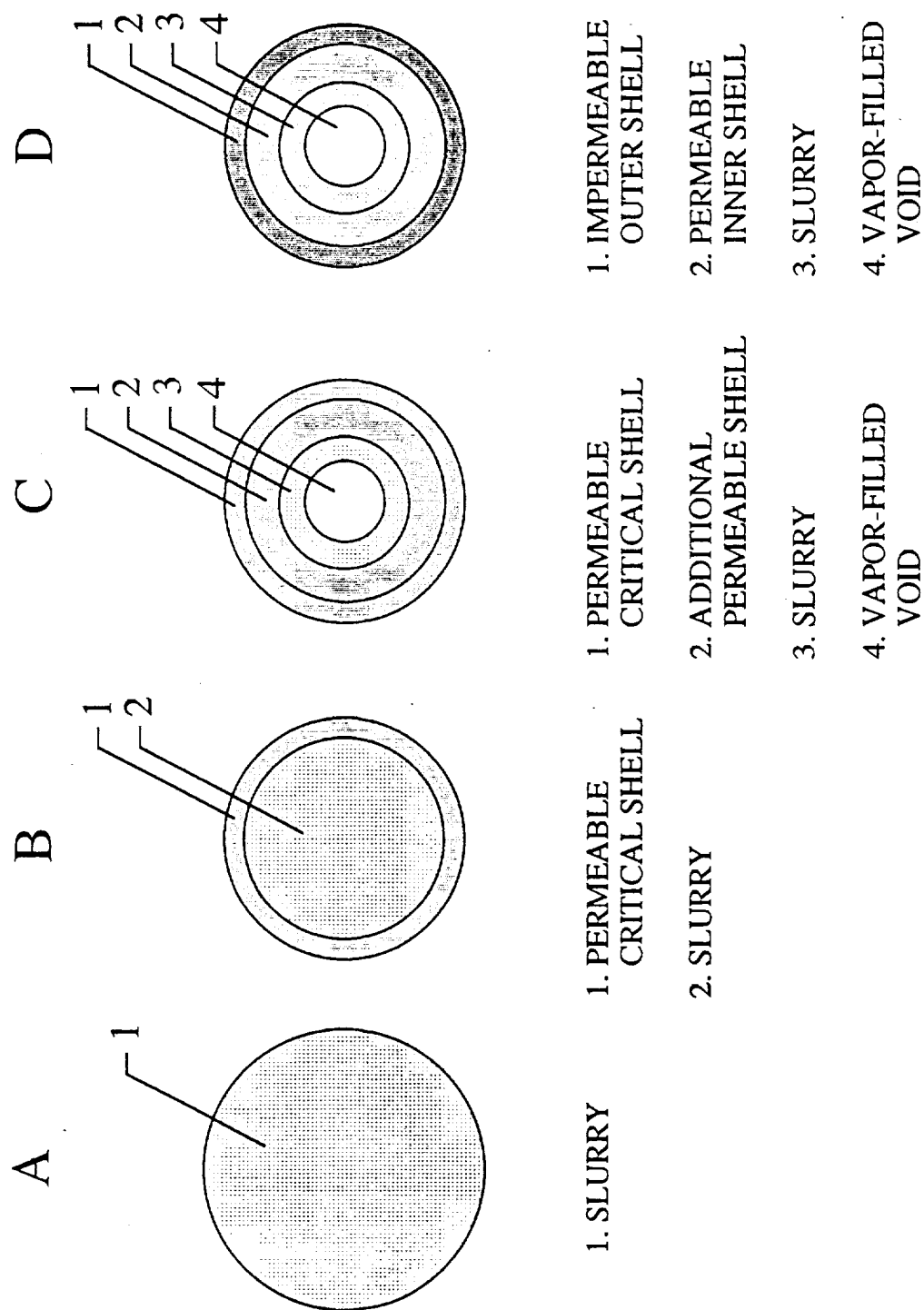


FIGURE 3. Schematic of critical shell formation, shell growth, vapor-void formation, and shell sealing.

The limiting number of particles required to form a rigid shell  $nd_u$  thick can be obtained by recognizing that the smallest possible shell diameter is just twice the rigid shell thickness,

$$d_{s,lim} = 2nd_u, \quad (4)$$

and using this result, the minimum number of particles to form a shell can be expressed

$$N_{p,lim} = 8\theta_{s,p} n^3. \quad (5)$$

The limiting initial droplet diameter can be obtained by setting  $N_{p,tot}$  [Eq. (1)] equal to  $N_{p,lim}$  [Eq. (5)] and solving for  $d_o$ :

$$d_{o,lim} = 2nd_u (\theta_{s,p} / \theta_{s,o})^{1/3}. \quad (6)$$

Equation (6) provides a criteria for determining whether a slurry drop of size  $d_o$  may undergo secondary atomization due to shell formation, provided the constituent particle size and initial solids loading are known. thus, for microexplosions to occur, we assume that

$$d_o > d_{o,lim}. \quad (7)$$

To evaluate Eq. (6), we assume that  $\theta_{s,p}$  is that of cubically packed spherical particles, while  $\theta_{s,o}$  is determined from  $Y_s$ ,  $\rho_s$ , and  $\rho_f$ , i.e.:

$$\theta_{s,p} = 0.524, \quad (8a)$$

$$\theta_{s,o} = \frac{\rho_f Y_s}{\rho_f Y_s + \rho_s (1 - Y_s)}. \quad (8b)$$

The preceding relationships [Eqs. (1)-(8)] were evaluated over a range of parameters including those associated with the slurry employed in the experimental portion of this investigation. Figure 4 shows  $d_{o,lim}$ , expressed as a multiple of constituent particle diameter,  $d_u$ , as a function of  $Y_s$ . Curves are shown for assumed shell thicknesses of 2, 3 and 4 times  $d_u$ . Experimental evidence [22,37] suggests that  $n=3$  is an appropriate value. As expected,  $d_{o,lim}$  decreases as  $Y_s$  increases [37]. The experimental 60 wt% Al slurry ( $d_u = 5 \mu m$ ) was predicted to have a  $d_{o,lim}$  of  $34.7 \mu m$ .

The dependence of the rigid shell diameter on initial droplet diameter and constituent particle size is shown in Fig. 5. Also indicated in the figure are the total number of particles and the fraction of these that go into forming the rigid shell. For example, an initial  $100 \mu m$  droplet with  $5 \mu m$  particles regresses to a rigid shell diameter of about  $82.6 \mu m$ , a decrease of 17.4 percent. A slightly greater percentage decrease in

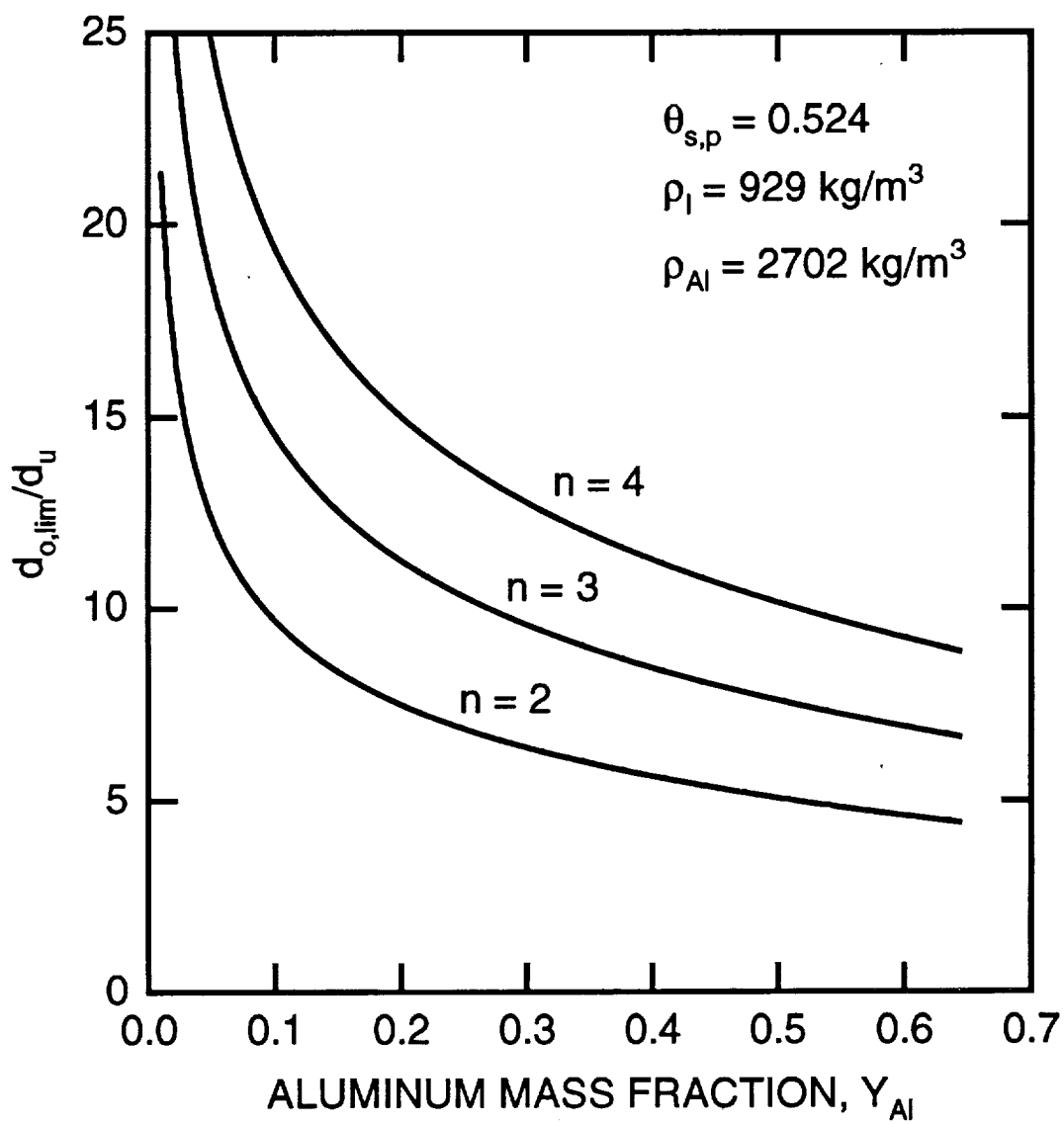


FIGURE 4. Dimensionless limiting initial diameter for the formation of a rigid shell as a function of aluminum mass fraction..

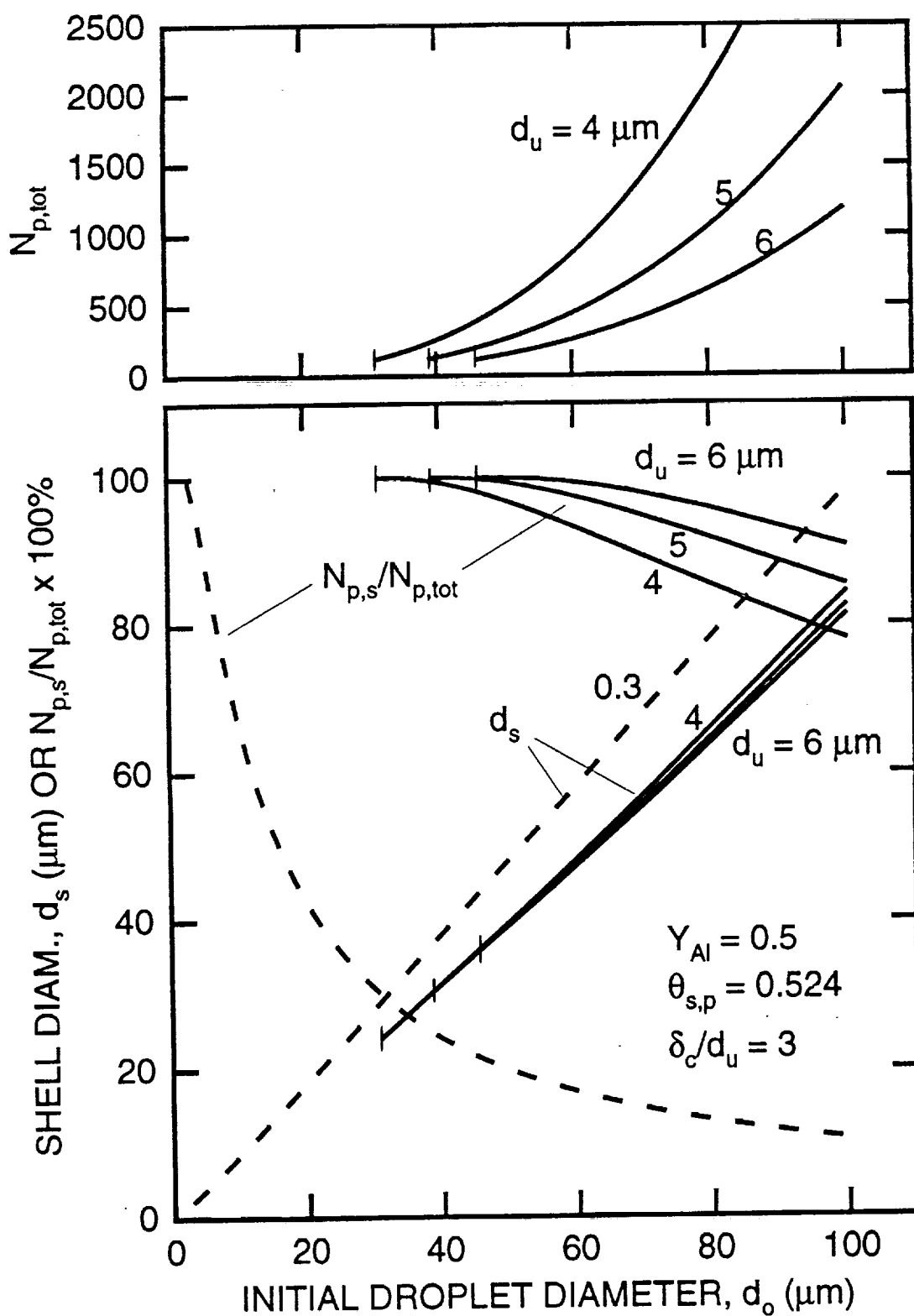


FIGURE 5. Shell diameter, fraction of total particles forming a critical shell, and the total number of particles versus initial droplet diameter.

diameter (21.3%) is found for a 40  $\mu\text{m}$  droplet. The limiting diameters and number of particles are indicated by the vertical lines at the left end of each curve. It is interesting to note that even for the largest aluminum slurry droplet investigated ( $d_o = 100 \mu\text{m}$ ), 78 to 90 percent of the total particles are required to form a shell. In contrast, boron and carbon slurries typically have much smaller constituent particles ( $d_u$  between 0.1 and 1  $\mu\text{m}$ ), and hence, a much smaller fraction of the total particles is present in the shell. To illustrate the differences between aluminum and carbon slurries, calculated shell diameter and fraction of solids in the shell for a carbon slurry are shown as dashed lines in Fig. 5. The carbon slurry had the same mass loading as the aluminum slurry, but  $d_u$  was 0.3  $\mu\text{m}$ . Here we see that very little diameter regression occurs and that the limiting initial diameter becomes quite small ( $d_{o,\text{lim}} = 2.15 \mu\text{m}$ ). Based on the results shown in Fig. 5, one would expect carbon slurries to exhibit disruptive burning behavior down to much smaller initial droplet sizes, compared to aluminum slurries.

**Disruption Model** - A conventional droplet vaporization analysis [38], modified to account for the solids [37], is employed to calculate droplet diameter, mass, and volume up to the critical shell formation time. During this period,

$$\frac{d(d_s)}{dt} = -2\dot{m} / (\pi \rho_f d_s^2) \quad (9)$$

with  $\dot{m}$  given by

$$\dot{m} = \frac{2\pi d_s k_g}{c_g} \ln \left[ \frac{c_g (T_\infty - T_b) + h_{fv} + c_f (T_b - T_o)}{h_{fv} + c_f (T_b - T_o)} \right] \quad (10)$$

In this particular approach, it is assumed that the surface temperature of the droplet is at the boiling point, which is a reasonable approximation.

Assuming constant properties, Eq. (9) can be integrated to yield

$$d_s^2(t) = d_o^2 - Kt \quad (11a)$$

where

$$K = \frac{8k_g}{\rho_f c_g} \ln(B+1) \quad (11b)$$

and

$$B = \frac{c_g (T_\infty - T_b)}{h_{fv} + c_f (T_b - T_o)} \quad (11c)$$

Since only the liquid evaporates,  $M$  is simply determined by the volume change, i.e.,

$$M(t) = M_o - \rho_f \pi (d_o^3 - d_s^3(t)) / 6 . \quad (12)$$

The shell formation time can be determined by substituting the value of  $d_s$  when the shell is  $nd_u$  thick into Eq. (11a). This value of  $d_s$  is readily calculated knowing  $\theta_{s,p}$  and  $\theta_{s,o}$  using Eqs. (1)-(3), as discussed previously.

In the period between  $t_c$  and  $t_s$ , we assume that evaporation continues at a rate equal to that at the instant of rigid shell formation, as has been done by other investigations [22,24,37]. A more exact treatment would have to deal with the complexities of flow through a porous medium that is not necessarily saturated with liquid [39,40]. In fact, it is only through a detailed treatment that takes into account local shell drying and the subsequent pyrolysis of the high boiling point surfactants that the processes leading to shell impermeability can be fully understood. Such a treatment is beyond the scope of the present work, and thus, the time interval  $t_s - t_c$  is treated as a parameter, which is varied to determine its effect.

During the period between  $t_c$  and  $t_s$ , the rigid shell grows in thickness and a vapor void forms. With the evaporation rate given by Eq. (10),  $d_p$  and  $d_v$  can be calculated by integrating simple mass and volume balances. The resulting expressions are [22]:

$$d_p^3 = (d_{s,c} - 2nd_u)^3 - \frac{3\theta_{s,o} d_{s,c} K(t_s - t_c)}{2(\theta_{s,p} - \theta_{s,o})} \quad (13)$$

$$d_v^3 = 3d_{s,c} K(t_s - t_c) / 2 \quad (14)$$

where the rigid shell is assumed to be wet with the liquid fuel. The vapor volume is directly determined from Eq. (14) as

$$V_v = \pi d_v^3 / 6 , \quad (15)$$

while the liquid volume is the total volume minus the vapor and solids volumes:

$$V_f = \pi (d_{s,c}^3 - \theta_{s,o} d_o^3 - d_v^3) / 6 . \quad (16)$$

Equations (15) and (16) provide two of the several initial conditions necessary to calculate the internal pressure history after the shell seals.

To gain some insights into the pressure build-up phenomena with a minimum of complexity, the solids-liquid-vapor system is treated as a single thermal lump, with the liquid and vapor existing as a saturated mixture of a single component fuel. Furthermore,  $d_{s,c}$  is assumed to be fixed; hence, total volume does not change as the pressure increases. For purposes of illustration, the properties of JP-10 are used. Energy conservation for the lumped system is expressed as

$$q_c = \frac{dU}{dt} = \frac{d}{dt}(M_v u_v + M_f u_f + M_s u_s). \quad (17)$$

Introducing the mixture quality, the liquid-vapor mixture internal energy is

$$U_m = M_v u_v + M_f u_f = M_m(u_f + xu_{fv}). \quad (18)$$

Treating the vapor phase as a pseudo-ideal gas with a constant compressibility factor,  $u_{fv}$  can be related to  $h_{fv}$ , as follows:

$$u_{fv} = h_{fv} - P\left(\frac{zRT}{P} - v_f\right). \quad (19)$$

For a rigid impermeable shell, the liquid-vapor system mass and volume are constant, hence

$$v = v_f + xv_{fv} = \text{constant} \quad (20)$$

Solving Eq. (20) for  $x$  and substituting the result into Eq. (18), together with the substitution of Eq. (19), yields

$$U_m = M_m \left\{ c_{pf} T + \frac{v - v_f}{\frac{zRT}{P} + v_f} \left[ h_{fv} - P\left(\frac{zRT}{P} - v_f\right) \right] \right\} \quad (21)$$

where we assume  $u_f = c_{pf}T$ .

The enthalpy of vaporization as a function of temperature can be approximated in terms of  $T_c$  and  $T_o$ , at which  $h_{fv,o}$  is known [41]:

$$h_{fv} = h_{fv,o} \left[ \frac{(1 - T/T_c)}{(1 - T_o/T_c)} \right]^{0.375}. \quad (22)$$

Since we are dealing with a wet mixture, the pressure and temperature are not independent properties. Thus, we employ the Clausius-Clapeyron equation to relate the saturation temperature and pressure, i.e.

$$P = A \exp(-B/T). \quad (23)$$

For JP-10,  $A$  has a value of  $3.069 \cdot 10^9$  Pascals, and  $B$  has a value of 4704.2 Kelvin [42]. Substituting Eq. (22) and (23) into Eq. (18) and differentiating with respect to time yields

$$\frac{dU_m}{dt} = M_m(\alpha_1 + \alpha_2 + \alpha_3) \frac{dT}{dt} \quad (24a)$$

where

$$\alpha_1 = c_{pf}, \quad (24b)$$

$$\alpha_2 = \frac{(v - v_f) \left[ \left( \frac{zRT}{P} - v_f \right) \beta - h_{fv} \frac{zR}{P} (1 - B/T) \right]}{\left( \frac{zRT}{P} - v_f \right)^2}, \quad (24c)$$

$$\alpha_3 = (v - v_f) A B \exp(-B/T) / T^2, \quad (24d)$$

and

$$\beta = \frac{-0.375 h_{fv,o}}{(T_c - T_o)^{0.375} (T_c - T)^{0.625}}. \quad (24e)$$

The liquid specific volume  $v_f$  has been assumed constant.

Substituting Eq. (24) into the energy balance (Eq. 17) for the solids-liquid-vapor system and solving for the temperature derivative yields

$$\frac{dT}{dt} = \frac{q_c}{[M_m(\alpha_1 + \alpha_2 + \alpha_3) + M_s c_{ps}]} \quad (25)$$

where it is assumed that  $u_s = c_{ps}T$ .

The integration of Eq. (25) provides the temperature history of the slurry droplet after the shell seals, and via the Clausius-Clapeyron relation (Eq. 23), the pressure history is determined. The instantaneous convective heat transfer rate is given by

$$q_c = h \pi d_{s,c}^2 (T_\infty - T). \quad (26)$$

Consistent with a fixed volume during pressure build-up, we assume that the microexplosion event is triggered by the failure of a brittle shell. For a thin shell, the internal stress level is readily calculated knowing the pressure difference across the shell:

$$\sigma = \frac{\Delta P r}{2\delta}. \quad (27)$$



**Model Results** - Figures 6 and 7 illustrate  $\delta$ ,  $M_f/M_{f,0}$ , and  $\sigma$  as functions of time after rigid shell formation for initial droplet sizes of 50 and 200  $\mu\text{m}$ , respectively. Thus, at time equals zero,  $\delta$  is  $3d_0$  or 15  $\mu\text{m}$ . For the 50  $\mu\text{m}$  drop-size, very little slurry remains after the critical shell is formed, so  $\delta$  grows only slightly ( $\sim 6\%$ ) as the remaining solids are added to the shell as the liquid evaporates. In contrast, the shell of the 200  $\mu\text{m}$  drop has the potential to increase up to 83% in thickness, if evaporation continues without the shell becoming impermeable and sealing the remaining fuel inside the shell.

The shell stress,  $\sigma$ , is shown as a family of three or four lines with each line corresponding to a different assumed shell sealing time. For example, in Fig. 6, the stress build-up is shown for assumed shell sealing times of 0.01, 0.2, and 0.5 ms. At the instant the shell seals, the mass fraction of the JP-10 becomes fixed and the pressure, and consequently the stress, begins to increase. For the 50  $\mu\text{m}$  droplet case, we see that the stress increases at essentially the same rate, regardless of the shell sealing time, as a consequence of the shell thickness being identical for each of the three histories shown. For the 200  $\mu\text{m}$  drop, the stress increases more rapidly for the earlier sealing times since the shells are thinner and have not yet reached their maximum thickness. We note also that stress levels increase with initial droplet diameter. This is a consequence of the larger mean shell radius, since the pressure levels for all cases ranged from an initial atmospheric value to 2000 kPa.

The above results imply that larger droplets are more likely to fragment than the smaller droplets because of higher shell stresses; and furthermore, the consequence of the larger drops' fragmenting is likely to be much more beneficial since the potential for spewing out raw slurry, rather than just producing shell fragments, is greater. In fact, for the 50  $\mu\text{m}$  droplet, only shell fragments can be produced if sealing occurs later than 0.01 ms after the critical rigid shell is formed.

### Limiting Drop Size for Disruption - Theory and Experiment

An experimental study was conducted to ascertain the minimum slurry drop size that would allow disruptive burning and the results were compared with predictions from the theory discussed above.

Size and ignition data for the 60 wt% slurry at  $x=5$ , 10, and 15 mm are presented in Fig. 8-11. Figures 8 and 9 show respective size distributions for a cold and a hot flow, 5 mm above the burner. The most obvious feature of Fig. 8 is the apparent bimodal particle size distribution. This distribution may be due to atomizing system characteristics or might be an artifact of the system collection bias since a PDF has not been applied to the data [32].

Before comparisons between experimental and theoretical results can be made, the axial location at which droplet combustion begins must be determined. Combustion is unlikely to start at the burner surface since the droplets must first pass through the cool, oxygen-deficient core of a diffusion flame above the central tube. Combustion is

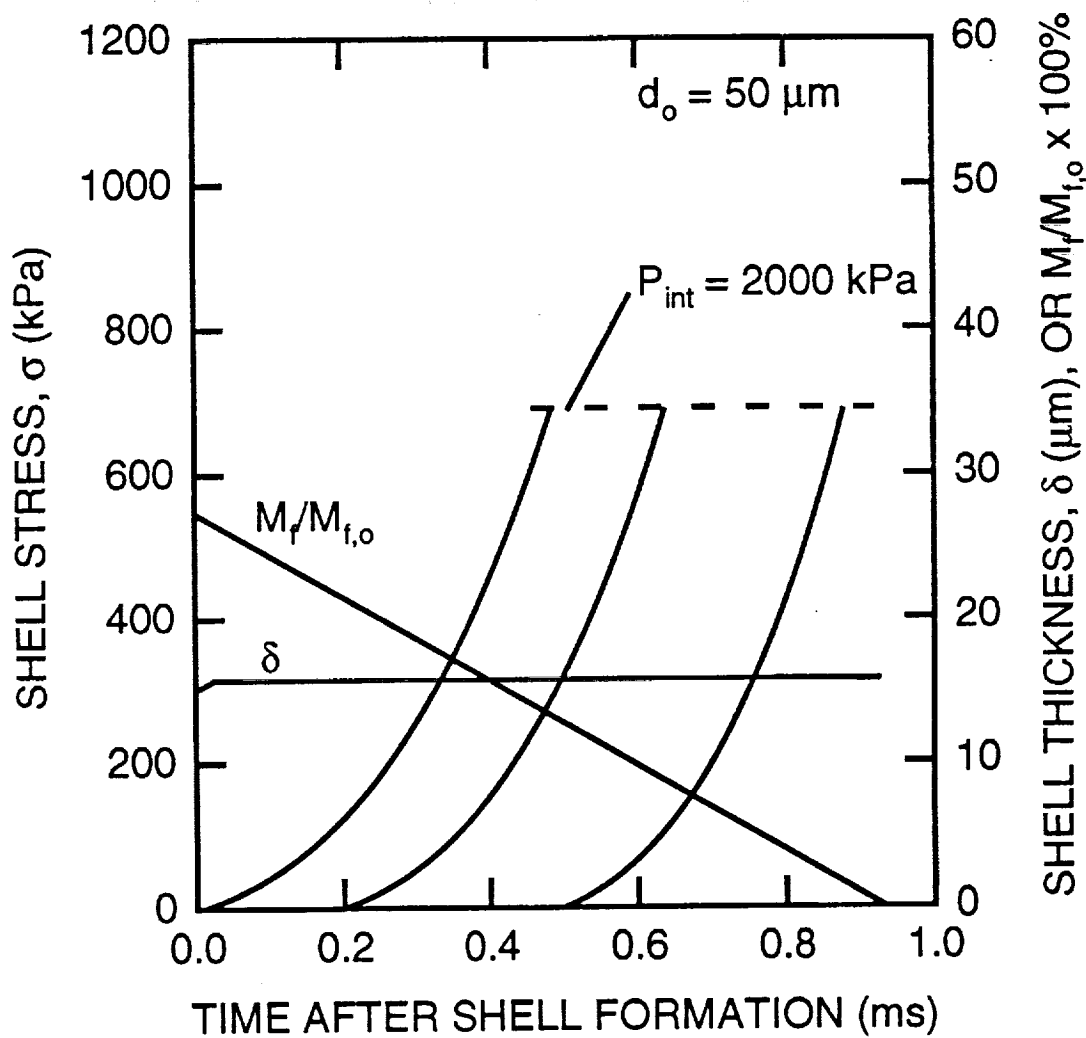


FIGURE 6. 50 wt% aluminum slurry droplet ( $d_o = 50 \mu\text{m}$ ) shell stress, liquid fuel mass fraction, and shell thickness as functions of time, assuming various shell sealing time intervals ( $d_{\text{ult}} = 5 \mu\text{m}$ ).

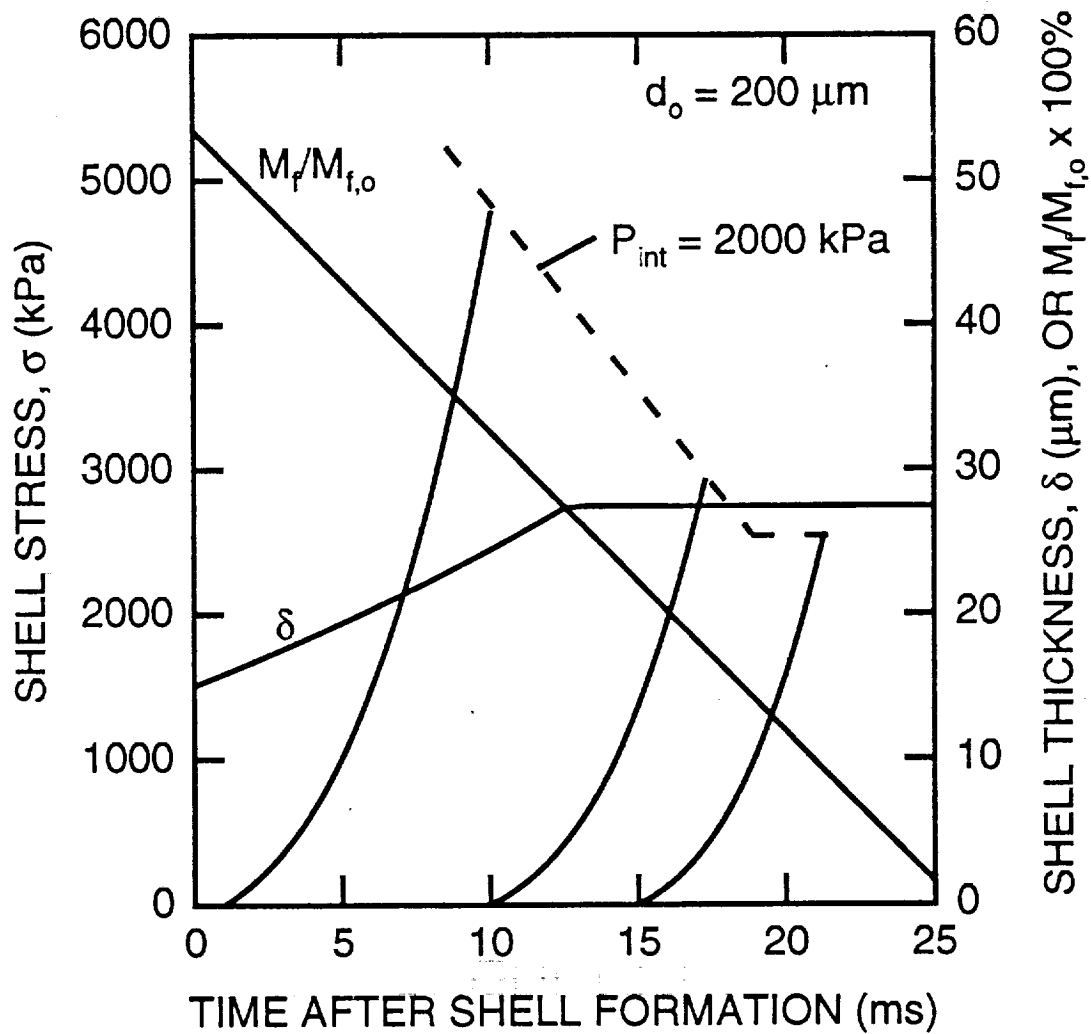


FIGURE 7. 50 wt% aluminum slurry droplet ( $d_o = 200 \mu\text{m}$ ) shell stress, liquid fuel mass fraction, and shell thickness as functions of time, assuming various shell sealing time intervals ( $d_{\text{ult}} = 5 \mu\text{m}$ ).

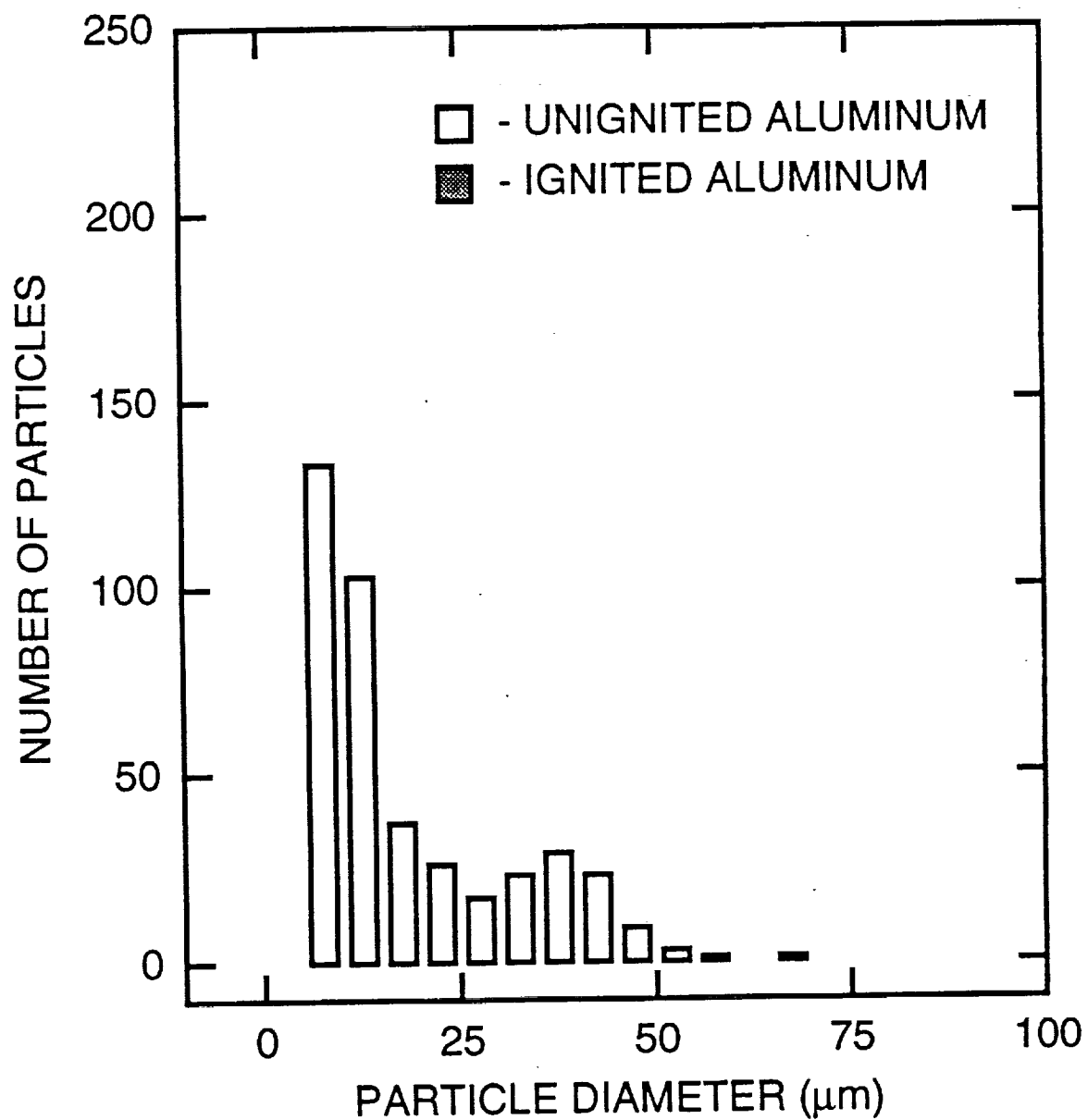


FIGURE 8. 60 wt% aluminum slurry particle size distribution 5 mm above the burner with no flame present.

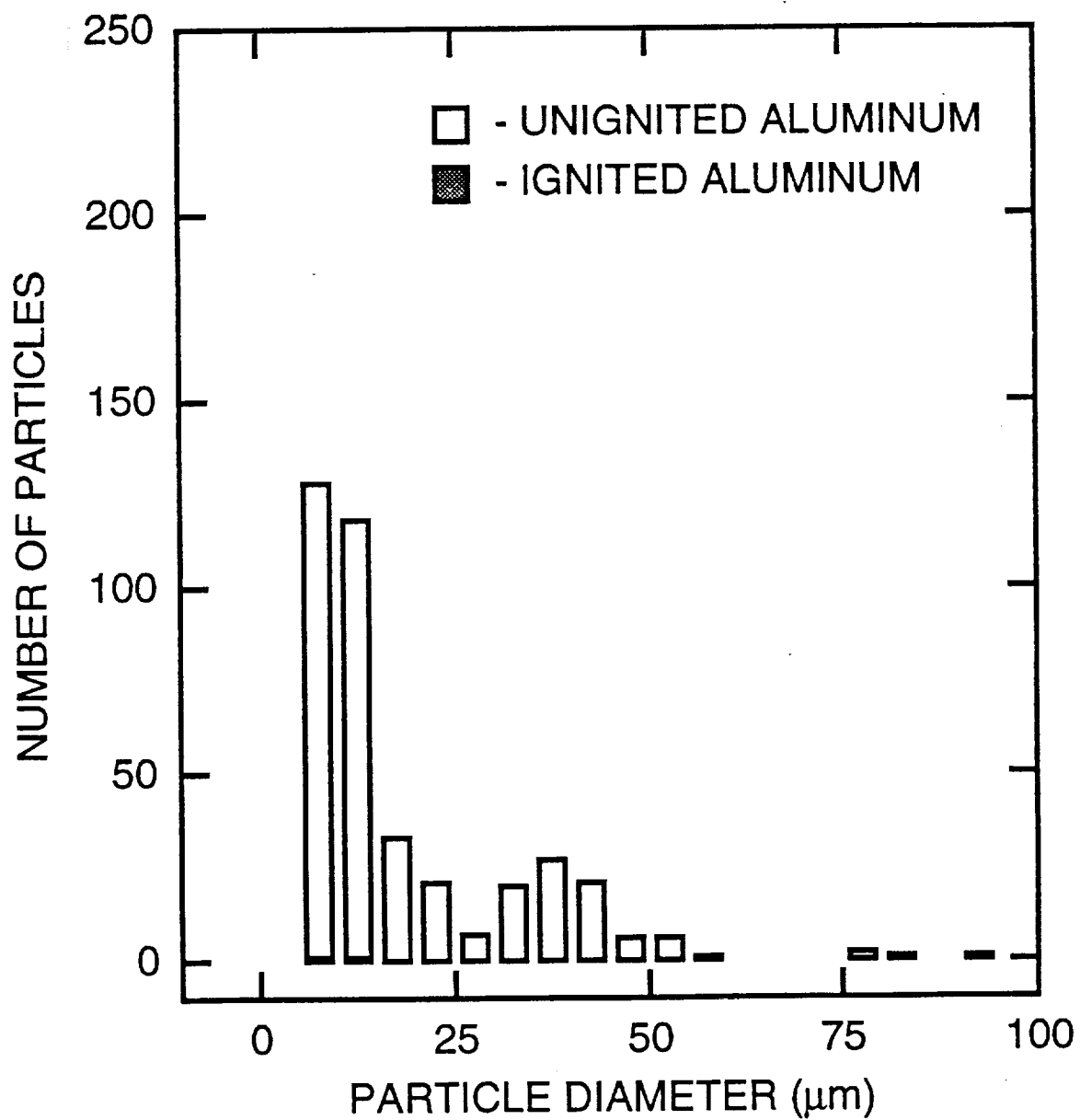


FIGURE 9. 60 wt% aluminum slurry particle size distribution 5 mm above the burner with flame present.

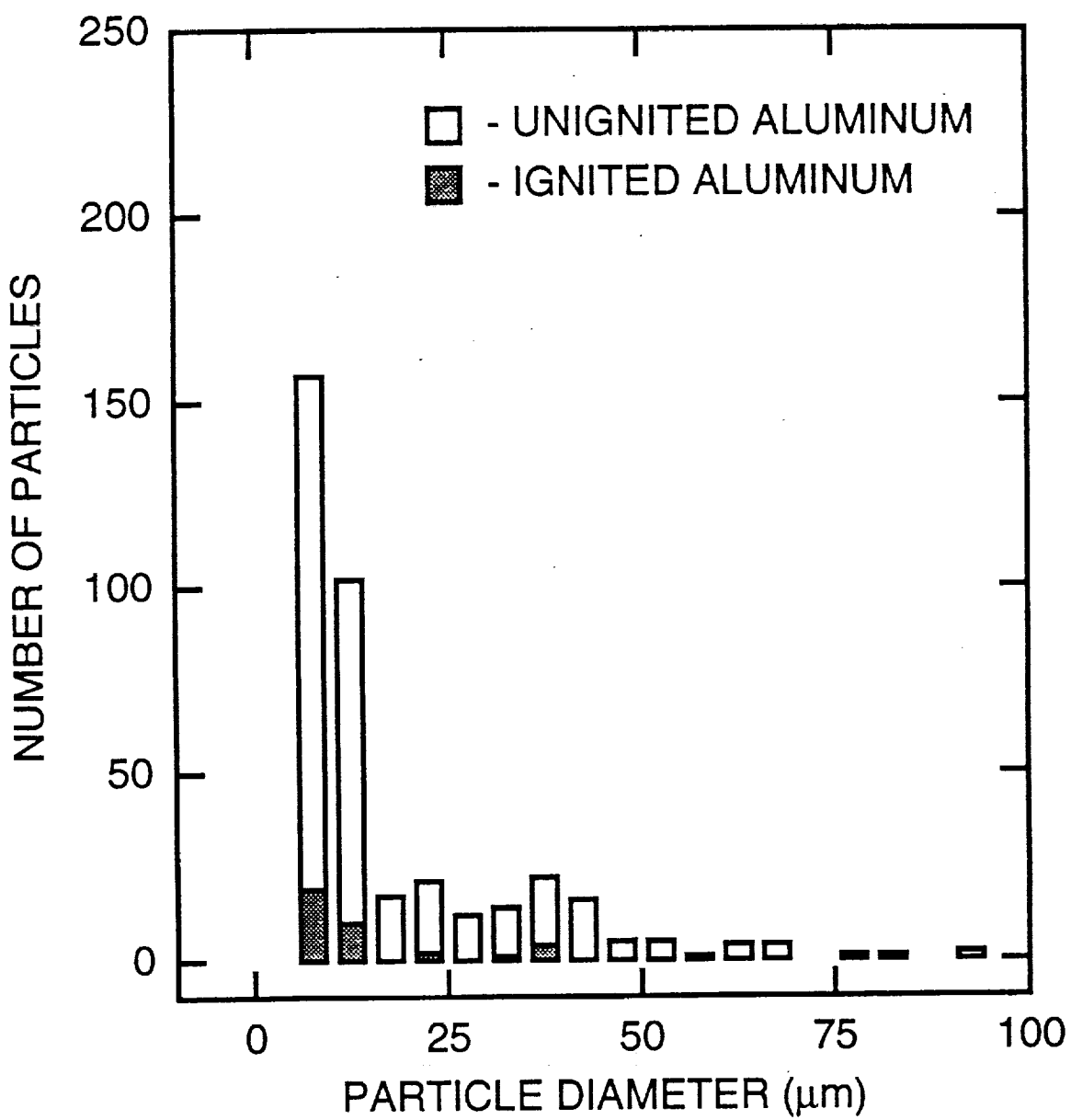


FIGURE 10. 60 wt% aluminum slurry particle size distribution 10 mm above the burner with flame present.

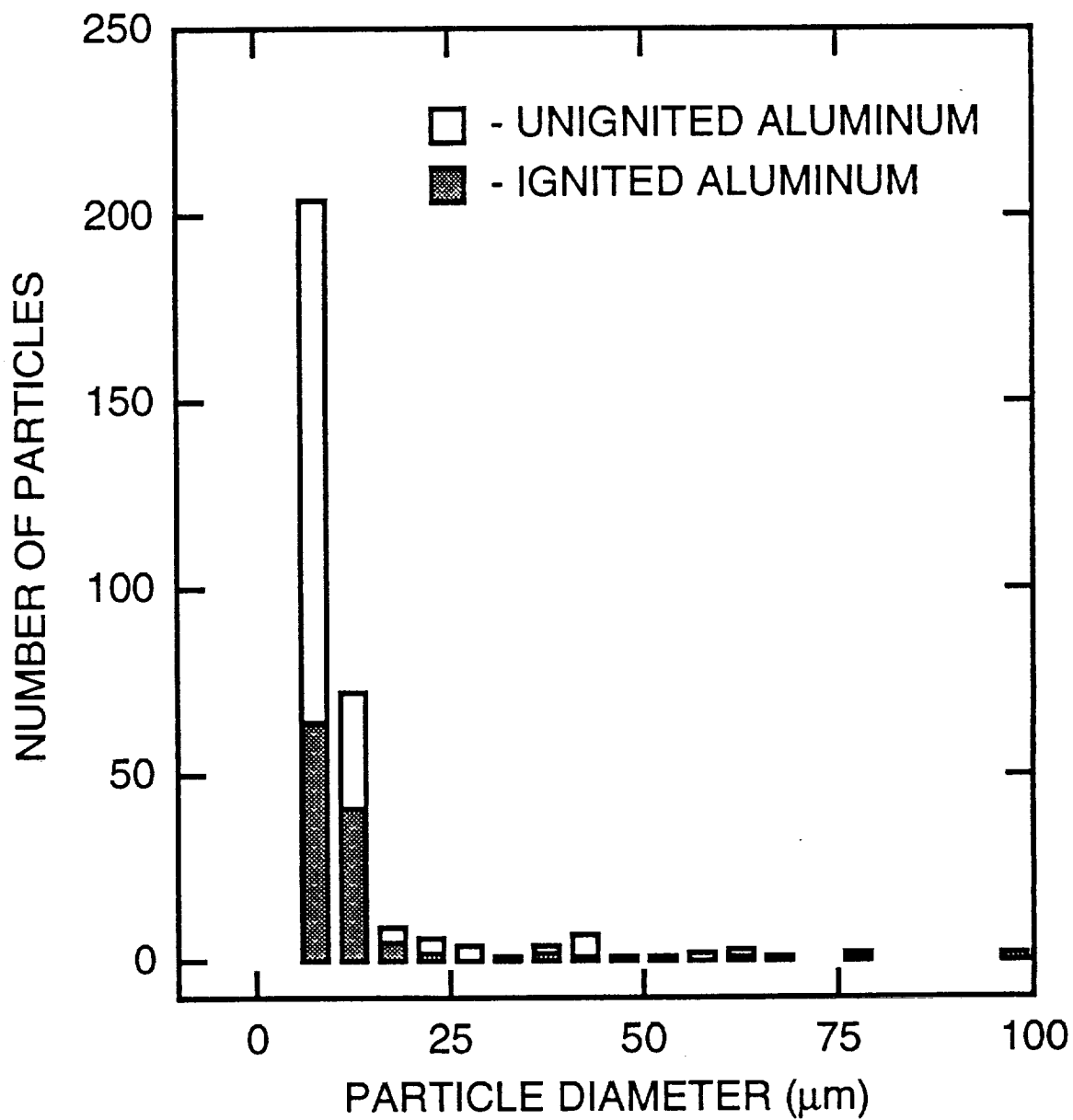


FIGURE 11. 60 wt% aluminum slurry particle size distribution 15 mm above the burner with flame present.

burner face as evidenced by the height of the surrounding burner flames. Figs. 8 and 9 instead likely to begin at the flame tip where heat and oxygen are present. Although the height of this flame is not clearly defined, the tip is between 3 and 7 mm above the burner face (x=5 mm), which show no major differences between the hot and cold flow size distributions, further support this premise of delayed droplet combustion activity.

The data in Fig. 10 (x=10 mm) show a slight shift toward smaller particles in comparison to the x=5 mm position. This is particularly visible in the 5-15  $\mu\text{m}$  range. Aluminum combustion is first seen to appear in this same size range, as would be expected, since faster liquid burnout results in shorter aluminum agglomerate ignition times for the small slurry droplets.

Figure 11 (x=15 mm) shows a sharp decrease in the number of particles in the 20-40  $\mu\text{m}$  range and a substantial increase in the number of particles in the 10-15  $\mu\text{m}$  region. These changes do not result from simple liquid evaporation since calculations indicate that agglomerates formed by 20-40  $\mu\text{m}$  droplets should give rise to an increase in particle number in the 20-30  $\mu\text{m}$  range rather than the 10-15  $\mu\text{m}$  range. These facts lead to the conclusion that secondary atomization of particles in the 20-40  $\mu\text{m}$  range occurs between the 10 and 15 mm axial locations. This conclusion is also consistent with visual observations of sudden bursts of glowing particles in this same region and higher in the flame, with very few below 10 mm.

Average particle velocities for the data in Figs. 8-11 were calculated to be approximately 7 m/s, ranging from 2-10 m/s. Assuming that particles travel at this average velocity and that droplet life histories begin 5 mm above the burner instead of at the burner face, as discussed above, then particles will reach the 10 mm axial location in 0.71 ms, and the 15 mm location in 1.4 ms. It is important to note that these calculated times-of-flight are highly sensitive to the location at which droplet combustion activity begins. With these assumptions, experimental results correlate reasonably well with prior theoretical analyses of aluminum agglomerate ignition times [18,19].

As mentioned above, Fig. 10 (x=10 mm) shows some aluminum combustion in the 5-10  $\mu\text{m}$  size range. The time for a particle to reach this axial location (t=0.7 ms) is comparable to calculated agglomerate ignition times. For example, calculations predict that a 14.3  $\mu\text{m}$  slurry droplet, forming a 10  $\mu\text{m}$  agglomerate, would require 0.6 ms for aluminum combustion to begin, agreeing favorably with the experimental value of 0.7 ms.

Since rigid shell formation is a precursor to secondary atomization, calculated rigid shell formation times should match observed disruption times if the shell sealing interval is short. Calculations show that a 40  $\mu\text{m}$  slurry droplet should form a rigid shell in 0.95 ms. This time interval falls between the particle times-of-flight required to reach the 10 mm location (t=0.71 ms), and the 15 mm location (t=1.4 ms). The sharp decrease in particle number in the 20-40  $\mu\text{m}$  range seen in Fig. 9 (x=15 mm) occurs in this same region. However, it is interesting to note that the lower end of this size range, 20  $\mu\text{m}$ , is somewhat less than the predicted  $d_{o,lim}$  of 34.7  $\mu\text{m}$ .



This discrepancy between experimental and theoretical minimum diameters could be due to experimental uncertainty in measuring particle size, primarily associated with the unknown slurry droplet index of refraction; however, light scattering in the near-forward direction is relatively insensitive to particle index of refraction. Another reason for this discrepancy may be that  $d_{o,lim}$  of  $34.7\text{ }\mu\text{m}$ , was calculated assuming a critical shell thickness of  $3d_u$  [22]. If this critical thickness is instead assumed to be only  $2d_u$ , then the predicted  $d_{o,lim}$  becomes  $24\text{ }\mu\text{m}$ , much nearer the experimentally measured limiting diameter of  $20\text{-}25\text{ }\mu\text{m}$ . A difference in critical shell thickness could be due to surfactants or particle morphology affecting particle binding. The critical shell thickness of  $3d_u$  was determined using a carbon slurry ( $d_u = 0.3\text{ }\mu\text{m}$ ) containing unknown surfactants and stabilizers. If these additives are different in type or concentration from our aluminum slurry, the shell formation characteristics may be affected. Similarly, if the ultimate particles in the carbon slurry were more uniform in size or smoother in shape, the shell formation processes could again be affected [24].

## One-Dimensional Combustion Chamber Model Development

**Overview** - Recent performance analyses of slurry fueled rockets [2-6] predict that Al slurry propellants may increase maximum payload over neat liquid systems. However, these studies neglect additional radiation and two-phase flow losses resulting from solid combustion products and increases in droplet combustion times due to solid agglomerate combustion. Accounting for these three factors is critical in accurately predicting the effects of using metallized propellants as rocket fuels.

The research discussed in previous sections of this report focuses on the mechanism of secondary atomization as a possible means of reducing combustion times and two-phase flow losses. However, this work is devoted to understanding the droplet combustion and secondary atomization processes themselves and does not involve the effects of secondary atomization on engine performance. Consequently, a one-dimensional engine model was developed to provide a preliminary evaluation of the effects of secondary atomization, two-phase flow losses, and radiation heat transfer on engine performance. Coding a new model for the combustion chamber provides some benefits over using a standard code such as TDK. First, the new model will permit the inclusion of secondary atomization effects, and second, the model will allow a clearer, if simpler, understanding of the physics involved in the problem. Therefore, a numerical code incorporating the following effects has been written to model a rocket combustion chamber:

- Multiple droplet size classes
- Gas-phase chemical equilibrium
- Two-phase flow losses
- Hydrocarbon evaporation and burnout

- Al combustion with surface condensation of  $\text{Al}_2\text{O}_3$
- Simple secondary atomization
- Radiation from condensed products to the chamber walls

Chamber dimensions and propellant flow rates have been taken from Galecki's work [43], to provide realistic model inputs.

**Model Description** - The propellants used in the engine model are a JP-10/Al slurry and a preheated gaseous  $\text{O}_2$  oxidizer. JP-10, a pure hydrocarbon ( $\text{C}_{10}\text{H}_{16}$ ), was chosen as the slurry hydrocarbon component instead of RP-1 to avoid the complexity of modeling multi-component droplet combustion.

The combustor flow is modeled using a single product-phase containing both gases and small  $\text{Al}_2\text{O}_3$  fume particles, and three additional flow phases for each droplet size class: a liquid hydrocarbon phase, an aluminum phase, and a phase containing large  $\text{Al}_2\text{O}_3$  agglomerates. The  $\text{Al}_2\text{O}_3$  must be separated into two flow phases because of the two oxidation mechanisms inherent in aluminum combustion [44-46]. In the first oxidation mechanism, large  $\text{Al}_2\text{O}_3$  agglomerates are formed through droplet surface condensation/oxidation, and in the second, very small  $\text{Al}_2\text{O}_3$  fume particles are produced through vapor-phase oxidation. Since the  $\text{Al}_2\text{O}_3$  agglomerates are much larger than the fume particles and are attached to the surface of the aluminum droplets it is necessary to model the  $\text{Al}_2\text{O}_3$  agglomerates separately from the fume particles. Including the fume particles in the gas-phase flow requires the assumptions of no temperature or velocity slip between the fume particles and the gases, but greatly simplifies the problem solution.

As an Al droplet burns, it continually produces  $\text{Al}_2\text{O}_3$  fume particles at the oxide boiling point which subsequently equilibrate with the gas-phase temperature and velocity. This process results in a range of fume particle temperatures and velocities as new particles are created and older particles continue to equilibrate with the gases. If the temperature and velocity slip were not neglected, many additional flow phases would be required to accurately model this range of fume particle temperatures and velocities. A detailed justification of the no-slip conditions is presented in Ref. [29].

**Mass Conservation** - For  $M$  droplet size classes, the following equation can be written for system mass conservation assuming steady-state conditions and that no mass is added to or removed from the chamber except at the injector face and the chamber exit:

$$\frac{d\dot{m}_g}{dx} = - \sum_{j=1}^M \left( \frac{d\dot{m}_{LH}}{dx} + \frac{d\dot{m}_{Al}}{dx} + \frac{d\dot{m}_{Al_2O_3}}{dx} \right)_j \quad (28)$$

In Eq. 28,  $x$  is axial position in the combustor;  $j$ , a particular droplet size class; and  $\dot{m}_g$ , the gas mass flux. The liquid hydrocarbon, aluminum, and  $\text{Al}_2\text{O}_3$  agglomerate mass fluxes for a particular droplet size class are given as  $\dot{m}_{LH}$ ,  $\dot{m}_{Al}$ , and  $\dot{m}_{Al_2O_3}$ ,

respectively. The terms on the right hand side of Eq. 28 are found from a hydrocarbon droplet gasification model and an aluminum droplet combustion model. The development of all three terms is similar and is outlined below.

The change in mass of a single slurry droplet in a size class,  $j$ , during a time interval  $dt$  is:

$$m_{\text{change},j} = \frac{dm_{\text{drop},j}}{dt} dt \quad (29)$$

where  $m_{\text{change},j}$  represents the hydrocarbon, aluminum, or  $\text{Al}_2\text{O}_3$  mass change. The value of  $dm_{\text{drop},j}/dt$  for the liquid hydrocarbon is found from the hydrocarbon gasification model while  $dm_{\text{drop},j}/dt$  for the aluminum and  $\text{Al}_2\text{O}_3$  are both determined from the aluminum combustion model. Relating  $dt$  to  $dx$  through the chain rule and the velocity relationship

$$u_{p,j} = \frac{dx}{dt} \quad (30)$$

yields

$$m_{\text{change},j} = \frac{dm_{\text{drop},j}}{dt} \frac{dx}{u_{p,j}}, \quad (31)$$

where  $u_{p,j}$  is the velocity of droplets in the  $j^{\text{th}}$  size class. This velocity is calculated through a drag analysis developed later in the report.

Equation 31 can be converted to a change in mass flux by multiplying  $m_{\text{change},j}$  by the total number of droplets in the  $j^{\text{th}}$  size class passing through the control volume per unit time,  $N/\tau_j$ . Substituting this result, Eq. 28 becomes

$$\frac{d\dot{m}_g}{dx} = - \sum_{j=1}^M \left[ \frac{N}{\tau_j} \frac{1}{u_{p,j}} \left\{ \left( \frac{dm_{\text{drop}}}{dt} \right)_{\text{LH}} + \left( \frac{dm_{\text{drop}}}{dt} \right)_{\text{Al}} + \left( \frac{dm_{\text{drop}}}{dt} \right)_{\text{Al}_2\text{O}_3} \right\} \right] \quad (32)$$

The value of  $N/\tau_j$  for each droplet size class can be determined from the total initial slurry mass flux and normalized droplet size distribution. Given an initial normalized droplet size distribution, it is necessary to determine  $N/\tau_{\text{total}}$  before  $N/\tau_j$  can be found for the individual size classes.  $N/\tau_{\text{total}}$  can be found from the following mass conservation expression:

$$\dot{m}_{\text{slurry},o} = \frac{N}{\tau_{\text{total}}} \sum_{j=1}^M \left( \tilde{N}_j \frac{1}{6} \rho_o \pi d_{j,o}^3 \right), \quad (33)$$

where  $\tilde{N}_j$  represents the percentage of total droplets in a given size class, given by the normalized size distribution. The variables,  $d_{j,0}$  and  $\rho_0$ , represent the initial diameter of the  $j^{\text{th}}$  size class and the initial slurry density, respectively. With  $N/\tau_{\text{total}}$  known,  $N/\tau_j$  for each size class can be calculated from

$$\frac{N}{\tau_j} = \tilde{N}_j \frac{N}{\tau_{\text{total}}} \quad (34)$$

Neglecting droplet breakup and secondary atomization,  $N/\tau_j$  is constant throughout the chamber. This leaves the following three variables for each size class to be determined from the droplet gasification models:  $(dm_{\text{drop},j}/dt)_{\text{LH}}$ ,  $(dm_{\text{drop},j}/dt)_{\text{Al}}$ ,  $(dm_{\text{drop},j}/dt)_{\text{Al}_2\text{O}_3}$ .

**Energy Conservation** - The steady-state energy balance for the system, including radiation heat losses, can be expressed as

$$\frac{d(\dot{m}h)_g}{dx} = \sum_{j=1}^M \left[ \frac{d(\dot{m}h)_{\text{LH}}}{dx} + \frac{d(\dot{m}h)_{\text{Al}}}{dx} + \frac{d(\dot{m}h)_{\text{Al}_2\text{O}_3}}{dx} \right] - 2\pi R q^r, \quad (35)$$

where  $h$  represents total specific enthalpy ( $h_{\text{chem}} + h_{\text{sens}}$ ),  $R$  is the chamber radius, and  $q^r$  is the radiation heat flux from the flow to the wall. Since gas flow optical properties are dominated by the small  $\text{Al}_2\text{O}_3$  fume particles [47], the radiation term is independent of the individual droplet size classes and is not included in the summation term.

Each of the bracketed terms on the right hand side of Eq. 35 can be expanded as

$$\frac{d(\dot{m}h)}{dx} \Big|_j = \left[ \dot{m} \frac{dh}{dx} + h \frac{d\dot{m}}{dx} \right]_j \quad (36)$$

Substituting for  $dm/dx$  yields

$$\frac{d(\dot{m}h)}{dx} \Big|_j = \left[ \dot{m} \frac{dh}{dx} + h \left( \frac{N}{\tau} \frac{1}{u_p} \frac{dm_{\text{drop}}}{dt} \right) \right]_j \quad (37)$$

Because the enthalpy required to heat the liquid hydrocarbon from 300K to the hydrocarbon boiling temperature (438.9 kJ/kg at  $P=6$  atm) is comparable to the hydrocarbon latent heat of vaporization (~286.7 kJ/kg at  $P=6$  atm), hydrocarbon heat up must be accounted for in the hydrocarbon vaporization model presented later in this report. In the vaporization model, the bulk droplet temperature is assumed to remain at the initial droplet temperature. Heat transfer from the gas heats a thin surface layer of

liquid hydrocarbon from the initial temperature to the boiling point and vaporizes this hydrocarbon layer. Using the constant bulk droplet temperature assumption yields a constant liquid hydrocarbon specific enthalpy, which reduces Eq. 37 for the liquid hydrocarbon to

$$\left. \frac{d(\dot{m}h)_{LH}}{dx} \right|_j = h_{LH,T_o} \left[ \frac{N}{\tau} \frac{1}{u_p} \frac{dm_{drop,LH}}{dt} \right]_j, \quad (38)$$

where  $h_{LH,T_o}$  is the liquid hydrocarbon specific enthalpy at the initial droplet temperature.

Following hydrocarbon burnout, an agglomerate of aluminum particles remains [18,19]. The aluminum agglomerate temperature rises from the hydrocarbon boiling temperature, through the aluminum melting point, to the aluminum boiling temperature as heat is transferred from the gas flow to the agglomerate. The enthalpy required for this temperature increase is significant compared to the total system enthalpy and the aluminum enthalpy of vaporization,  $h_{fv,Al}$ . Consequently, agglomerate ignition/heat up should be modeled. The agglomerate ignition/heat-up process is approximated as convective heat transfer from the gas flow to a spherical, uniform-temperature agglomerate. Heat transfer to the agglomerate causes the agglomerate temperature to rise from the hydrocarbon boiling temperature to the aluminum melting temperature. The agglomerate temperature is then held constant until sufficient energy to melt the entire agglomerate has been transferred from the gas-flow, at which point aluminum combustion begins. For the heat-up and phase-change processes, the general energy conservation equation (cf. Eq. 37) using the above assumptions reduces to

$$\left. \frac{d(\dot{m}h)_{Al}}{dx} \right|_j = \left[ \dot{m} \frac{dh}{dx} \right]_j = \left[ \dot{m} \frac{N}{\tau} \frac{1}{u_p} \left( \frac{A_p \bar{h} (T_g - T_{Al})}{m_{drop,Al} c_{p,Al}} \right) \right]_j, \quad (39)$$

where  $\bar{h}$  is the average heat-transfer coefficient.

After the agglomerate phase-change, Eq. 37 for the aluminum mass flux becomes

$$\left. \frac{d(\dot{m}h)_{Al}}{dx} \right|_j = h_{Al,T_{m,Al}} \left[ \frac{N}{\tau} \frac{1}{u_p} \frac{dm_{drop,Al}}{dt} \right]_j, \quad (40)$$

where  $h_{Al,T_{m,Al}}$  is the liquid aluminum specific enthalpy at the melting temperature.

Since  $Al_2O_3$  agglomerate forms on the aluminum droplet surface, the  $Al_2O_3$  agglomerate is maintained at the aluminum boiling temperature as long as any aluminum remains in the droplet. For the time period prior to aluminum burnout, Eq. 37 reduces to

$$\left. \frac{d(\dot{m}h)_{Al_2O_3}}{dx} \right|_j = h_{Al_2O_3, T_{b,Al}} \left[ \frac{N}{\tau} \frac{1}{u_p} \frac{dm_{drop, Al_2O_3}}{dt} \right]_j \quad (41)$$

for the  $Al_2O_3$  agglomerate, where  $h_{Al_2O_3, T_{b,Al}}$  is the  $Al_2O_3$  specific enthalpy at the aluminum boiling temperature. After aluminum burnout, the  $Al_2O_3$  agglomerate mass remains constant but heat transfer to or from the gas flow causes the agglomerate temperature to change. Following the development for aluminum heat up (Eq. 39), Eq. 37 reduces to

$$\left. \frac{d(\dot{m}h)_{Al_2O_3}}{dx} \right|_j = \left[ \dot{m} \frac{dh}{dx} \right]_j = \left[ \dot{m} \frac{N}{\tau} \frac{1}{u_p} \left( \frac{A_p \bar{h} (T_g - T_{Al_2O_3})}{m_{drop, Al_2O_3} c_{p, Al_2O_3}} \right) \right]_j \quad (42)$$

for the  $Al_2O_3$  agglomerates during the time period after aluminum burnout. The total system energy balance (Eq. 35) is represented by appropriate substitutions of Eqns. 38-42.

**Radiation Heat Transfer** - Radiation from the solid combustion products to the chamber wall is a participating medium phenomena requiring the solution of the radiative-transfer equation. Given a scattering albedo, the transfer equation can be solved numerically, but requires a great deal of computer time. Fortunately, the transfer equation can be simplified and solved using one of several approximations based on the value of the optical thickness,  $K_D$ , which is define as

$$K_D = \int_0^S (a + \sigma_s) ds = \int_0^S \kappa ds, \quad (43)$$

where  $a$  and  $\sigma_s$  are the absorption and scattering coefficients, respectively, and  $S$  is the characteristic radiation path length. If  $\kappa$ , defined as  $(a + \sigma_s)$ , is constant along this path,  $K_D$  can be expressed as

$$K_D = \kappa S. \quad (44)$$

$Al_2O_3$  smoke optical properties are used in evaluating the transfer equation since the smoke particles dominate the gas flow optical properties as discussed earlier in the report. Parry and Brewster [47] determined the optical properties of  $Al_2O_3$  smoke produced by a solid propellant containing 20% aluminum by mass, burning at a 1.8 MPa pressure. Optical thicknesses,  $K_D = 1.28$  at  $\lambda = 632.8$  nm and  $K_D = 1.21$  at  $\lambda = 1064$  nm, were found for the 1 mm thick smoke region. Assuming a constant  $\kappa$  in the transmission direction, Eq. 44 produces  $\kappa = 1280$  and  $\kappa = 1210$  for  $\lambda_1$  and  $\lambda_2$ , respectively.

Although the above  $\kappa$  values were obtained from a solid propellant flame, they should provide a first approximation of the gas flow optical thickness in the model

combustion chamber. Given that  $\kappa$  is a function of fume volume fraction,  $\kappa$  actually may be greater for aluminum slurry combustion than for the above solid propellant due to the higher slurry aluminum mass percentage. As a conservative estimate, Parry and Brewsters'  $\kappa$  values will be used in estimating a minimum gas flow optical thickness.

In the model, chamber radius,  $R = 0.025$  m, is the characteristic path length. Using this radius, the optical thickness is between 30 and 32. These values are much greater than  $K_D = 2.0$ , which is considered the lower limit for an optically-thick medium [51]. Therefore, as a first estimate, the gas flow can be treated as an optically-thick medium, in which local radiation heat transfer is only influenced by the immediate surroundings. Based on this optical thickness, a diffusion approximation [51] can be used to simplify the radiative transfer equation. The cylindrical  $P_1$  diffusion approximation [52] has been chosen since it provides greater accuracy than other approximations, yet is still simple to incorporate. A detailed development of this radiation model is presented in Ref. [29]. The final result of this analysis for the radiant heat transfer rate from the particles to the wall of a cylindrical chamber with radius,  $R$ , is

$$q^r(R) = \frac{4\pi(I_{bf} - I_{bw})I_1\left(\frac{R}{\xi}\right)}{\left[3\xi I_0\left(\frac{R}{\xi}\right) + 2I_1\left(\frac{R}{\xi}\right)\right]}, \quad (45)$$

where

$$\xi = \frac{1}{\sqrt{3(1-\Omega_o)}}, \quad (46)$$

and  $\Omega_o$  is the scattering albedo,

$$\Omega_o = \frac{\sigma_s}{a + \sigma_s} \quad (47)$$

where  $I_0(R/\xi)$  and  $I_1(R/\xi)$  are the modified Bessel functions

$$I_v\left(\frac{R}{\xi}\right) = \sum_{k=0}^{\infty} \frac{\left(\frac{R}{2\xi}\right)^{2k+v}}{k! \Gamma(K+v+1)}, \quad (48)$$

where  $v$  equals 0 or 1.

Since  $\Omega_o$ , and therefore  $\xi$ , is a function of wavelength,  $\lambda$ , the radiant heat transfer rate (Eq. 45) must be integrated over all wavelengths as follows:

$$q^r(R) = \int_0^{\infty} \frac{4\pi(I_{bf}(\lambda) - I_{bw}(\lambda))}{3\xi I_o(R/\xi) + 2I_1(R/\xi)} \cdot I_1(R/\xi) d\lambda. \quad (49)$$

If  $\xi(\lambda)$  is assumed to be constant in a wavelength interval, Eq. 49 can be expressed as the following summation:

$$q^r(R) = \sum_{n=1}^L \left[ \frac{4I_1(R/\xi_n)}{3\xi_n I_o(R/\xi_n) + 2I_1(R/\xi_n)} \cdot (F_{\lambda_{n+1}-\lambda_n}(T_f) \sigma T_f^4 - F_{\lambda_{n+1}-\lambda_n}(T_w) \sigma T_w^4) \right] \quad (50)$$

where  $F_{\lambda_{n+1}-\lambda_n}(T)$  is the fraction of total radiation emitted by a blackbody at temperature  $T$  in the wavelength interval between  $\lambda_{n+1}$  and  $\lambda_n$ .

The absorption and scattering cross-sections,  $C_a$  and  $C_s$  are determined from Mie theory for each of the  $M$  wavelength regions in Eq. 49. The absorption and scattering coefficients,  $a$  and  $\sigma_s$ , are determined from the following relations [51]:

$$a = C_a N \quad (51a)$$

$$\sigma_s = C_s N \quad (51b)$$

where  $N$  is the number density of fume particles, and it has been assumed that the  $Al_2O_3$  fume particles are uniform in size.

**Momentum Conservation** - The gas-phase momentum equation in the combustion chamber is trivial, assuming a negligible chamber pressure gradient and no body forces. The negligible chamber pressure gradient condition should be accurate for current conditions, but does require the assumption of no wall frictional losses or pressure drops due to flow acceleration. However, the momentum equations governing the hydrocarbon, aluminum, and agglomerate  $Al_2O_3$  mass fluxes are significant. In a given slurry droplet, there is no slip between the hydrocarbon and the aluminum before hydrocarbon burnout, and no slip between the aluminum and the  $Al_2O_3$  agglomerate afterwards; therefore, the hydrocarbon aluminum and  $Al_2O_3$  agglomerate momentum equations in a given droplet size class can be reduced to a single momentum equation. Virtual mass and Bassett forces can be neglected since the particle density is much greater than the gas density. The particle momentum equation for a droplet size class can be expressed as

$$\vec{F} = m \vec{a}, \quad (52)$$

where  $\vec{F}$  is the drag force on a particle,  $m$  is the particle mass and  $\vec{a}$  is the particle acceleration,  $du_p/dt$ . Substituting for the drag force using a drag coefficient,  $C_D$ , and using the chain rule to relate  $du_p/dt$  to  $du_p/dx$  results in the following form of Eq. 52:



$$\frac{du_p}{dx} = \frac{3 \rho_g C_D (u_g - u_p) |u_g - u_p|}{4 \rho_p d u_p} \quad (53)$$

In this equation,  $\rho_g$  is the gas density,  $u_g$  the gas velocity,  $u_p$  the droplet velocity,  $\rho_p$  the droplet density, and  $d$  the droplet diameter.

The drag coefficient is approximated as that of a sphere using the following correlation [52]:

$$C_D = \frac{24}{Re} + \frac{6}{(1 + \sqrt{Re})} + 0.4, \quad (54)$$

where the Reynolds number,  $Re$ , is based on the slip velocity between the gas and the droplet.

**Slurry Combustion** - The physics of slurry droplet combustion and a probable secondary atomization process are described above and in other references [18-20,24,37]. After hydrocarbon burnout occurs in a droplet or the droplet fragments, the remaining agglomerate(s) of aluminum particles heats up, melts to form a single molten aluminum droplet, and burns.

Cho and Takahashi's shell formation model [37] is used to predict the droplet diameter at which rigid shell formation occurs for each droplet size class in the combustor model. When running the combustor code, it is assumed that secondary atomization occurs when the droplet diameter reaches the predicted rigid-shell diameter. Although secondary atomization actually occurs some time after rigid shell formation, the time interval presently is not known and is therefore, neglected in the combustor model. However, future experimental efforts should provide an estimate of this time interval, and then the time interval will be included in the combustor model.

Particle size distribution after secondary atomization is also currently an unknown to be determined from experimental measurements and is treated as a system variable. In the combustor model, a droplet undergoing secondary atomization is presently assumed to shatter into a specified number of equal-size secondary droplets. Defining the fragmentation ration,  $\beta$ , as the number of secondary droplets produced per initial droplet, a new value of  $N/\tau_j$  can be expressed as

$$\left. \frac{N}{\tau} \right|_{j,new} = \beta \left. \frac{N}{\tau} \right|_{j,old} \quad (55)$$

Knowing the slurry mass flux of a given size class,  $\dot{m}_{slurry,j}$ , a new size class droplet diameter,  $d_{j,new}$ , can be found from the mass conservation expression,

$$\dot{m}_{\text{slurry},j} = \frac{N}{\tau}\bigg|_{j,\text{new}} \frac{\pi}{6} d_{j,\text{new}}^3 \quad (56)$$

Because of the close proximity of the slurry droplets to each other, the droplets are not surrounded by individual flames. Therefore, droplet combustion can be modeled as an evaporation process. Detailed development of the hydrocarbon gasification problem are presented in Ref. [29]. The final mass balance for the droplet is

$$\frac{dm_{\text{drop,LH}}}{dt} = -\frac{4\pi k_g r_s}{c_{p,g}} \ln \left[ \frac{c_{p,g}(T_g - T_b)}{h_{fV,LH} + \int_{T_o}^{T_{\text{boil}}} c_{p,LH} dT} + 1 \right], \quad (57)$$

which is used in the system mass and energy governing equations.

As mentioned previously, aluminum combustion proceeds through two different oxidation mechanisms; the first is aluminum vapor oxidation, and the second is droplet surface condensation/oxidation. A simple aluminum combustion model, based on previous research [19], was developed and incorporated into the combustor code [29]. Because aluminum agglomerate heating was treated as a simple step change in agglomerate temperature from the hydrocarbon temperature to the aluminum boiling temperature [29], droplet heating was neglected in the aluminum combustion model [29]. Recently, modeling of the aluminum agglomerate heating process has been improved as described earlier in this report (cf. Eq. 39). However, agglomerate heating from the hydrocarbon temperature to the aluminum boiling temperature is now separated into two stages. In the first stage, the agglomerate is heated to a molten state at the aluminum melting temperature [Eq. 39]. In the second stage, droplet heat-up during combustion brings the droplet from the aluminum melting temperature to the aluminum boiling temperature. This droplet heat-up is represented in the aluminum combustion model as the heating of a thin droplet surface layer from the aluminum melting temperature to the aluminum boiling temperature. This representation closely parallels the surface layer heat-up in the hydrocarbon vaporization model [29], and is therefore, not detailed in this report. The final result is

$$\frac{dm_{\text{drop,Al}}}{dt} = -\frac{4\pi k_g r_s}{c_{p,g}} \ln \left[ \frac{c_{p,g}(T_f - T_b)}{\left( h_{fV,Al} - \eta h_{fV,Al_2O_3} + \int_{T_{m,Al}}^{T_{b,Al}} c_{p,Al} dt \right)} + 1 \right], \quad (58)$$

where  $\eta$  is the fraction of the aluminum oxide that condenses, or is formed, at the droplet surface. It should be noted that  $h_{fV,Al_2O_3}$  is not a true enthalpy of vaporization since  $Al_2O_3$  does not exist in a gaseous state. Rather, it dissociates into  $2Al + 3/2O_2$ . Therefore,  $h_{fV,Al_2O_3}$  is actually the enthalpy released by the chemical reaction,  $2Al_{(g)} + 3/2O_2 \rightarrow Al_2O_{3(1)}$ , occurring at the droplet surface temperature.

**Solution Method** - Equations 32, 35, 53, 57, and 58 form the governing equation set and are numerically integrated in the axial direction using the IMSL integration routine DVERK [53] to determine  $\dot{m}_g$ ,  $(\dot{m}h)_g$ ,  $u_p$ ,  $\dot{m}_{LH}$ ,  $\dot{m}_{Al}$ , and  $\dot{m}_{Al_2O_3}$ . These values are then used to determine the gas temperature,  $T_g(x)$ , the radiation heat flux,  $q(x)$ , final  $Al_2O_3$  agglomerate diameter, and chamber burnout length. Initial conditions are supplied at the injector face. Reference [29] provides a description of the methods employed to determine the various required thermodynamic and transport properties.

## One-Dimensional Model Results

The one-dimensional engine code was exercised using the chamber diameter, pressure, flow rates, and aluminum mass loading presented in Table I. These values were chosen to simulate Galecki's test conditions [43]. Presently, chamber length is varied to allow complete propellant combustion. In the present study, an arbitrary normalized droplet size distribution is used (Fig. 12).

Table 1  
Model Operating Conditions

Chamber Diameter	0.0522 m
Chamber Pressure	690 kPa
Slurry Flow Rate	0.00142 kg/s
Aluminum Loading	60%
Oxidizer Flow Rate	0.00312 kg/s

Secondary atomization effects on combustion chamber gas and droplet velocities can be seen in Figs. 13 and 14. The data in Fig. 13 were calculated assuming no secondary atomization while the data in Fig. 14 assume a fragmentation ratio,  $\beta$ , of 40. In both cases, smaller droplets equilibrate more rapidly with the gas velocity than large droplets, and the gas velocity increases along the combustor axis due to decreasing gas density as temperature rises and mass addition to the gas flow from the slurry droplets.

As expected, droplet velocities are the same in both cases until secondary atomization occurs, after which, the slope of the Fig. 14 velocity profiles decreases sharply and the droplet velocities rapidly equilibrate with the gas velocity. This rapid equilibrium is caused by secondary atomization shattering the initial droplets into small secondary droplets which equilibrate with the gas velocity more quickly than the initial droplet could.

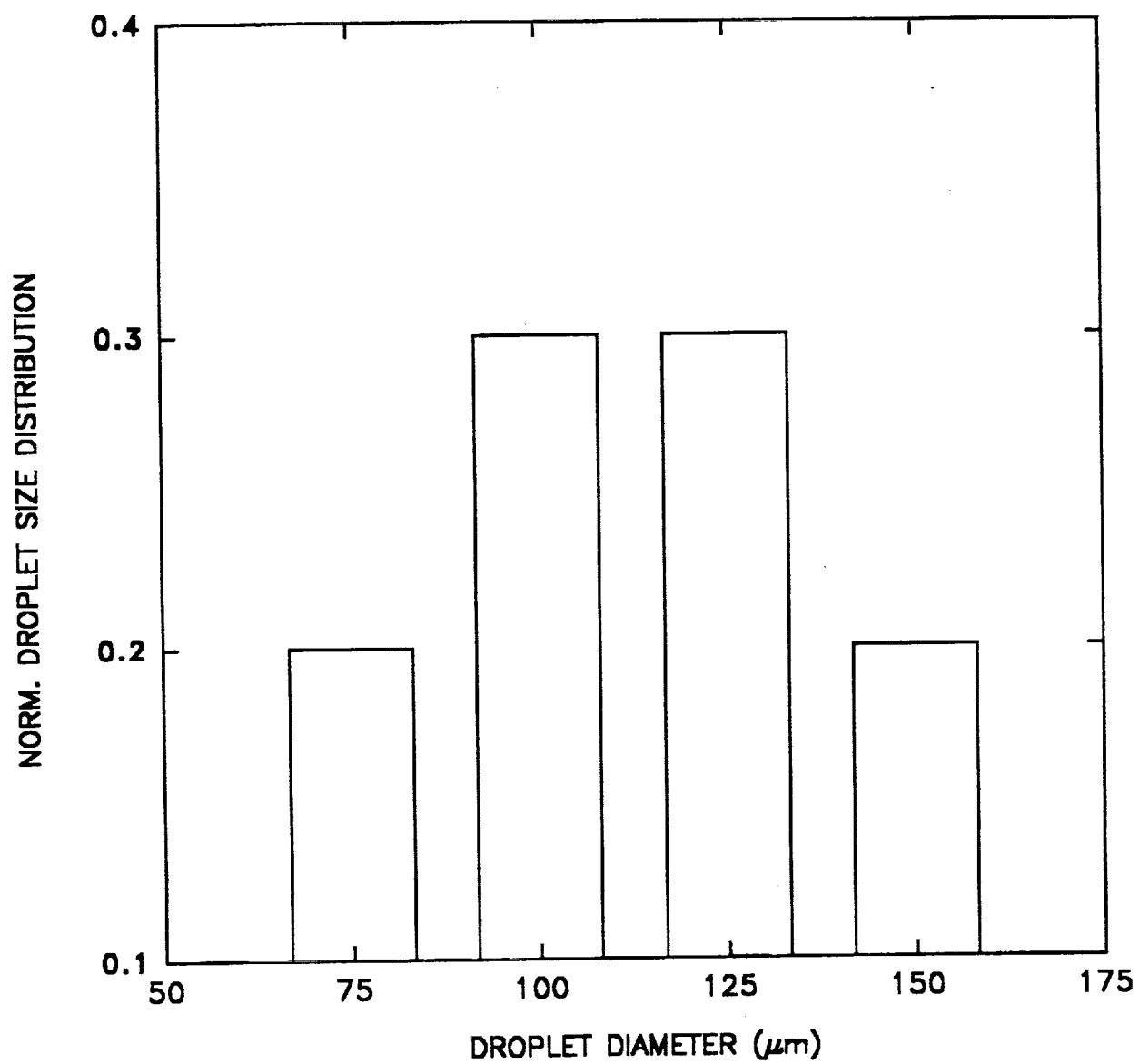


FIGURE 12. Normalized droplet size distribution used in combustor code.

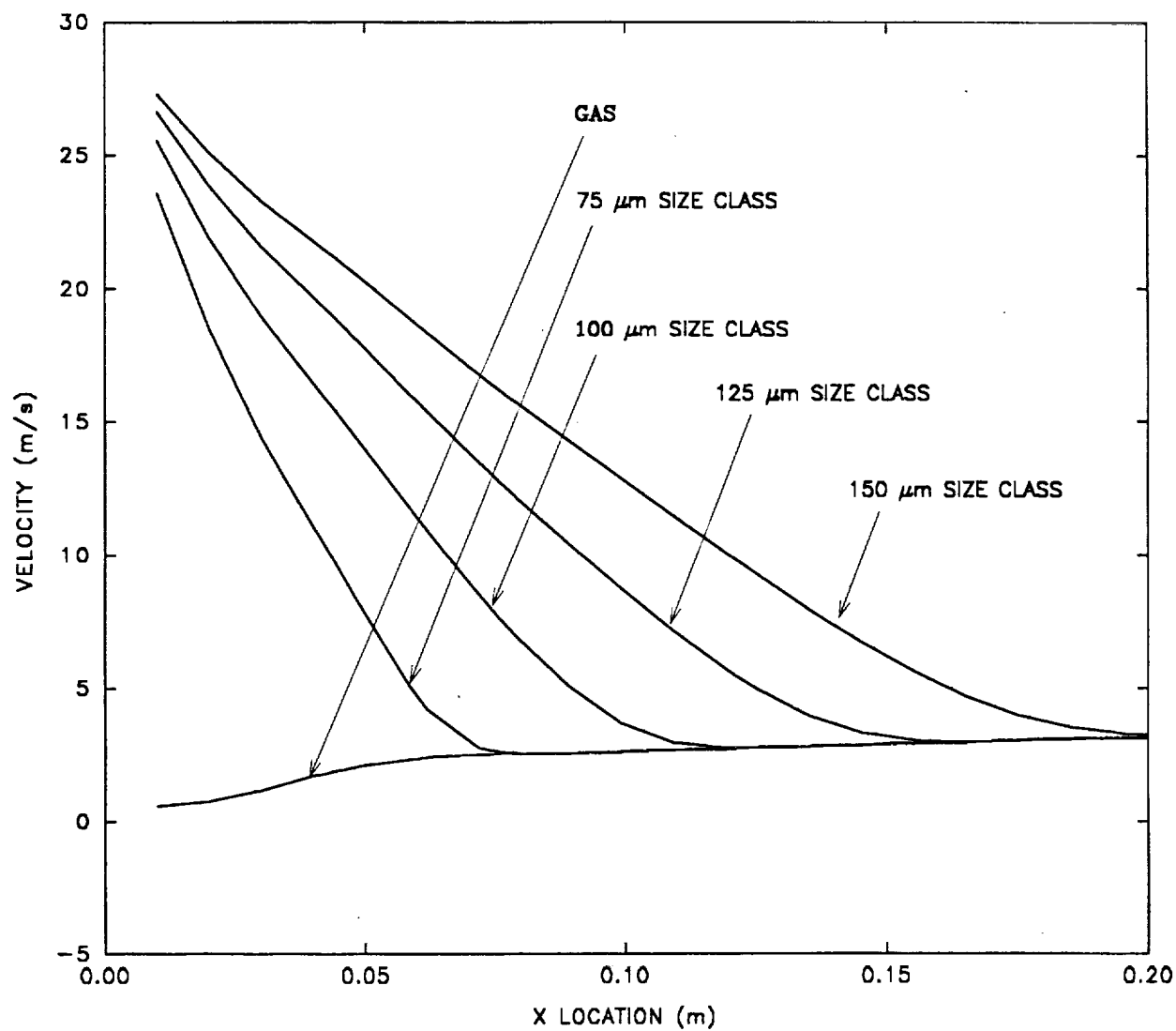


FIGURE 13. Gas and droplet velocities versus axial location for a 60 wt% Al slurry assuming no secondary atomization.

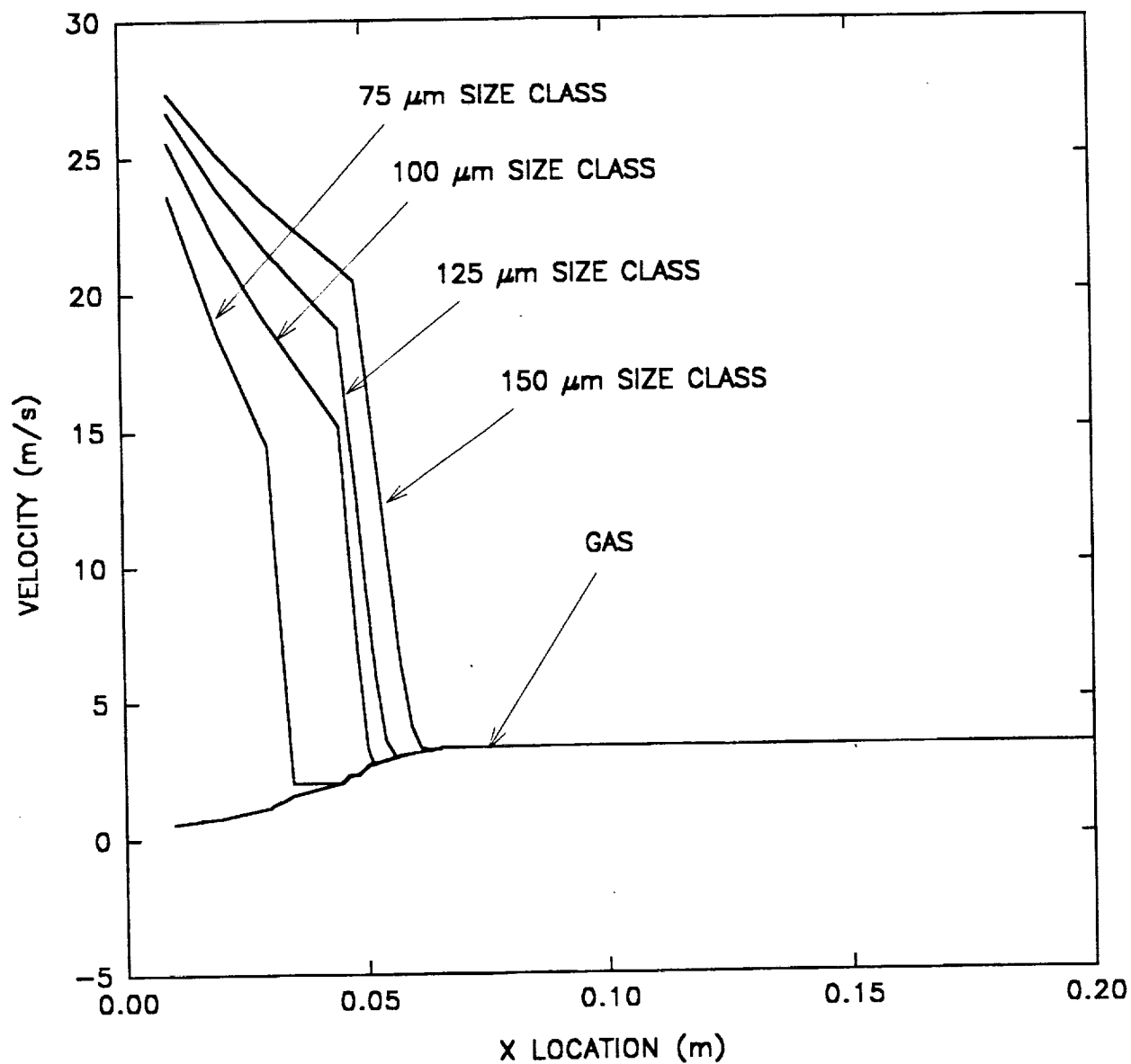


FIGURE 14. Gas and droplet velocities versus axial location for a 60 wt% Al slurry assuming no secondary atomization fragmentation ratio of 40.

Gas temperature and composition using a fragmentation ratio of five, are presented in Fig. 15. The jagged shapes of both the temperature and composition profiles arise from using only four droplet size classes instead of a continuous droplet size distribution. The inflection in the temperature profile between 0.05 and 0.15 m is caused by the large enthalpy transfer from the gas flow to heat the aluminum after hydrocarbon burnout. The composition plots show that the flow is fuel lean, as evidenced by excess  $O_2$  present after propellant burnout, and that  $CO_2$  and  $H_2O$  undergo dissociation due to the high gas temperature.

In Fig. 16, chamber burnout distance is plotted versus fragmentation ration,  $\beta$ , to illustrate the benefits of secondary atomization. It is readily apparent that only slight secondary atomization is required to yield significant decreases in droplet lifetimes. Higher secondary atomization intensities, represented by larger fragmentation ratios, have a lesser effect on burnout length because droplet lifetime is inversely proportional to droplet surface area, which increases as  $(\beta)^{2/3}$ .

Final oxide agglomerate diameter as a function of secondary atomization intensity,  $\beta$ , is shown in Fig. 17. Similar to the trend seen in Fig. 16, small secondary atomization intensities significantly reduce final  $Al_2O_3$  agglomerate diameters, with greater atomization intensities providing decreasing marginal reductions in diameter. However, final particle diameter is proportional to  $(1/\beta)^{1/3}$  and not  $(1/\beta)^{2/3}$  as was droplet lifetime.

The above results demonstrate that the combustor model produces realistic results, given current model assumptions, and that only low secondary atomization intensities are required to significantly decrease chamber burnout length and final particle size.

## SUMMARY AND CONCLUSIONS

Experimental and analytical methods were applied to obtain an improved understanding of the ignition and secondary atomization processes associated with aluminized hydrocarbon propellants. A numerical model of a rocket combustion chamber was also developed to help ascertain the influence of secondary atomization on combustor performance. The principal accomplishments and conclusions of our investigations are the following:

1. Apparatus and experimental techniques were developed to study the secondary atomization of slurry droplets in the 10-200  $\mu m$  diameter size range. Specifically, non-intrusive optical methods were implemented to measure droplet size and velocity, and to detect aluminum combustion of free-flying droplets in a high-temperature environment.
2. Models of slurry droplet disruption (secondary atomization) were applied to aluminum/liquid hydrocarbon propellants and show the following:

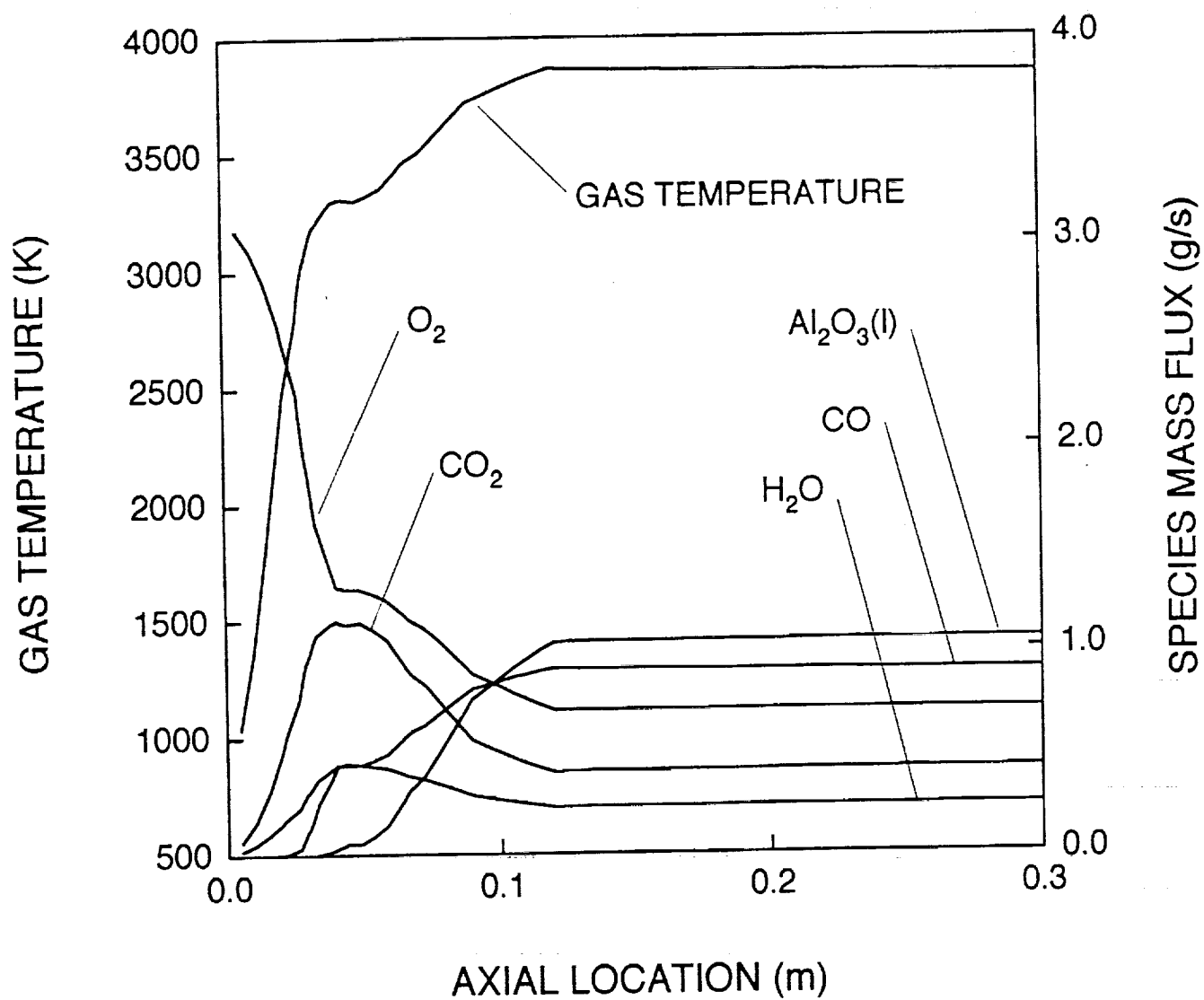


FIGURE 15. Mass flux of major gas species and gas temperature versus axial location. Data is for a 60 wt% Al slurry assuming a secondary atomization fragmentation ratio of 5.



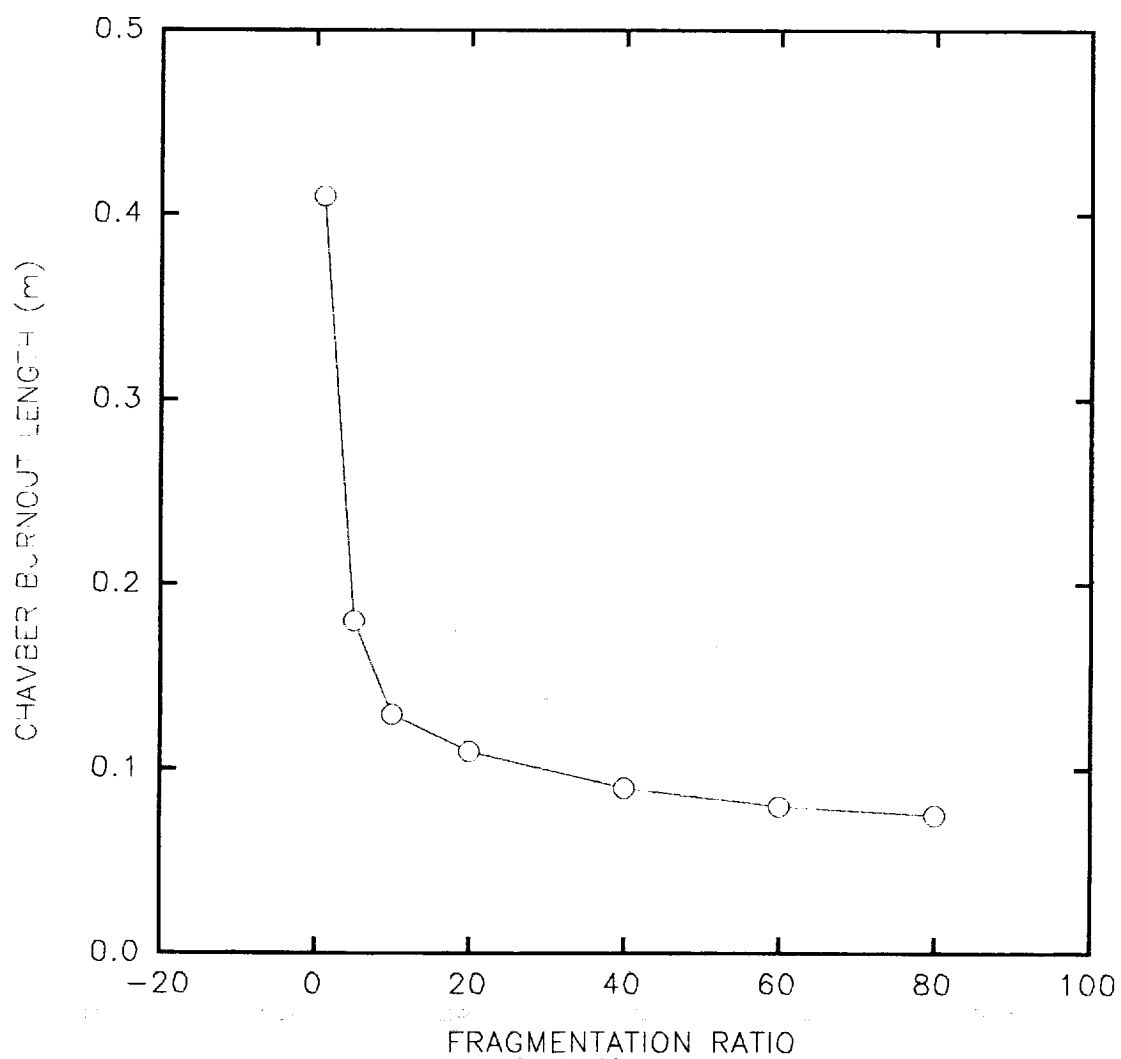


FIGURE 16. Chamber burnout distance as a function of secondary atomization fragmentation ratio for a 60 wt% Al slurry.

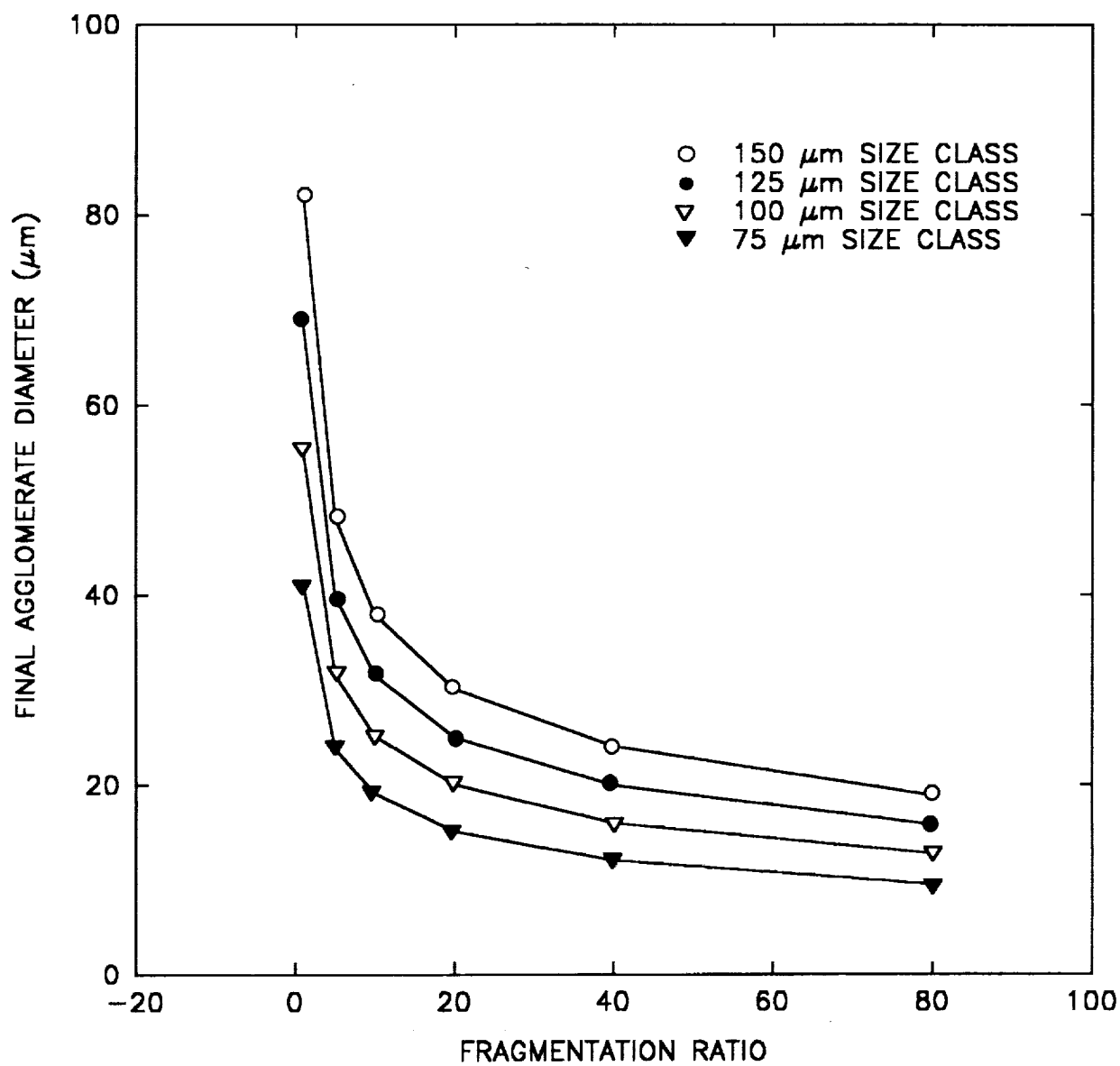


FIGURE 17. Final oxide agglomerate diameter as a function of secondary atomization fragmentation ratio. Data is for a 60 wt% Al slurry.

- Increasing solids mass fractions and decreasing ultimate particle diameter are predicted to significantly decrease the minimum slurry droplet diameter required to form a rigid shell, thereby reducing the minimum diameter required for secondary atomization.
  - Slurry droplets close to the minimum diameter for rigid shell formation should contain little or no liquid slurry after shell sealing and larger droplets should contain a significant amount of liquid slurry upon shell sealing. Therefore, secondary atomization may be less effective in the smaller droplets since only shell fragments, rather than secondary slurry droplets, are produced.
  - For small droplets ( $d_o < 50 \mu\text{m}$ ), shell stress is predicted to increase at essentially the same rate, regardless of the shell sealing time, as a consequence of constant shell thickness. In contrast, the stress in larger droplets was found to increase more rapidly for earlier sealing times since the shells are thinner at these shorter times, indicating that short sealing times may lead to rapid secondary atomization.
3. Theoretical calculations, based on a critical rigid shell thickness of three ultimate particles, predict a larger minimum slurry droplet diameter ( $d_{o,\text{lim}} = 34.7 \mu\text{m}$ ) required for disruption than was observed in the experimental data ( $d_{o,\text{lim}} = 20\text{--}25 \mu\text{m}$ ). This could be due to experimental uncertainties associated with the unknown slurry particle index of refraction or the critical shell thickness required for rigid shell formation.
  4. Calculated agglomerate ignition times were found to be in reasonable agreement with experimental results.
  5. A one-dimensional model of a rocket combustion chamber incorporating multiple droplet size classes, gas-phase chemical equilibrium, two-phase flow, hydrocarbon vaporization, aluminum combustion, simple secondary atomization, and radiation heat transfer was developed. Exercise of the model predicts the following:
    - Only moderate secondary atomization is required to effectively reduce overall propellant burn times and final  $\text{Al}_2\text{O}_3$  residual size. Greater secondary atomization intensities provide little additional benefit.
    - Preliminary results indicate that radiation losses to the chamber walls are less than 3% and should be even less in a full-size engine because of increases in combustion chamber diameter, and consequently, the flow optical thickness.

## ACKNOWLEDGMENTS

The authors would like to acknowledge the contributions of M.J. Scott to the development of the experimental systems and the technical support of L.L. Schaaf. The word processing skills of L.M. Palmer are also appreciated. This work was supported in part by the Propulsion Engineering Research Center under NASA Grant NAGW-1356.

## REFERENCES

1. Pinns, M., Olson, W., and Barnett, H., Breitwieser, R., "NACA Research on Slurry Fuels," NASA Report 1388, 1958.
2. Palaszewski, B.A., "Lunar Missions Using Advanced Chemical Propulsion: System Design Issues," AIAA Paper 90-2431, July 1990.
3. Palaszewski, B., "Metallized Propellants for the Human Exploration of Mars," NASA Technical Paper 3062, Nov. 1990.
4. Palaszewski, B., "Advanced Launch Vehicle Upper Stages Using Liquid Propulsion and Metallized Propellants," NASA Technical Memorandum 103622, Oct. 1990.
5. Zurawski, R.L., and Green, J.M., "An Evaluation of Metallized Propellants Based on Vehicle Performance," AIAA Paper 87-1773, June-July 1987.
6. Rapp, D.C., "High Energy-Density Liquid Rocket Fuel Performance," AIAA Paper 90-1968, July 1990.
7. Yatsuyanagi, N., *et al.*, "Combustion Characteristics of Metallized Hydrocarbon Fuels," 17th International Symposium on Space Technology and Science, Tokyo, Japan, May 1990.
8. Yatsuyanagi, N., "Combustion Characteristics of Metallized Hydrocarbon Fuels," *Japan Society for Aeronautical and Space Sciences*, Vol. 37, No. 420, 1989, pp. 393-399.
9. Schaplowsky, R.K., Anderson, R.E., Cabaal, J.A., and Vander Wall, E.M., "Characterization of Gelled RP-1 Containing Aluminum," JANNAP Propellant Development and Characterization Subcommittee Meeting, 1989.
10. Rapp, D.C., and Zurawski, R.L., "Characterization of Aluminum/RP-1 Gel Propellant Properties," AIAA Paper 88-2821, July 1988.
11. Sterns, R.S., and Hall, L.W., Jr., "Aluminum Slurry Fuel Formulation and Combustion," AFWAL-TR-88-2052, Nov. 1988.
12. Inamura, T., Nagai, N., Hirai, T., and Asamo, H., "Disintegration Phenomena of Metallized Slurry Fuel Jets in High Speed Air Stream," to be published.

13. Aitken, A.J., "Metallized Thixotropic Propellants," BSD-TDR-63-122 (DTIC AD-338493), June 1963.
14. Galecki, D.L., "Ignition and Combustion of Metallized Propellants," AIAA Paper 89-2883, July 1989.
15. Carbone, H.M., and Reese, B.A., "Studies of Slurry Fueled Propulsion Systems," ONR TM-74-4 (AD-779 895), Jan. 1974.
16. Peleg, I., and Timnat, Y.M., "Combustion of Aluminum and Boron Slurry Fuels in a Dump Combustor," *Nineteenth Symposium (International) on Combustion*, The Combustion Institute, 1982, pp. 557-563.
17. Cohen, J.D., and Howell, S.J., "Aluminum Slurry Fuel Combustion Technology," AFWAL-TR-85-2021, May 1985.
18. Wong, S.-C., and Turns, S.R., "Ignition of Aluminum Slurry Droplets," *Combust. Sci. and Tech.*, Vol. 52, 1987, pp 222-242.
19. Turns, S.R., Wong, S.-C., and Ryba, E., "Combustion of Aluminum-Based Slurry Agglomerates," *Combust. Sci. and Tech.*, Vol. 54, 1987, pp. 299-318.
20. Wong, S.-C., and Turns, S.R., "Disruptive Burning of Aluminum/Carbon Slurry Droplets," *Combust. Sci. and Tech.*, Vol. 66, 1989, pp. 75-92.
21. Wong, S.-C., Lin, A.-C., and Chi, H.-Y., "Effects of Surfactant on the Evaporation, Shell Formation, and Disruptive Behaviors of Slurry Droplets," *Twenty-Third Symposium (International) on Combustion*, The Combustion Institute, Pittsburgh, 1990, p. 1391-1397.
22. Lee, A., and Law, C.K., "Gasification and Shell Characteristics in Slurry Droplet Burning," *Combust. Flame*, Vol. 85, 1991, pp. 77-93.
23. Takahashi, F., Dryer, F.L., and Williams, F.A., "Combustion Behavior of Free Boron Droplets," *Twenty-First Symposium (International) on Combustion*, The Combustion Institute, Pittsburgh, 1986, pp. 1983-1991.
24. Takahashi, F., Heilweil, I.J., and Dryer, F.L., "Disruptive Burning Mechanism of Free Slurry Droplets," *Combust. Sci. and Tech.*, Vol. 65, 1989, pp 151-165.
25. Turns, S.R., Mueller, D.C., and Scott, M.J., "Ignition and Combustion Characteristics of Metallized Propellants," Semi-Annual Report (June 1989-Dec. 1989) to NASA Lewis Research Center, January 1990.
26. Turns, S.R., Mueller, D.C., and Scott, M.J., "Ignition and Combustion Characteristics of Metallized Propellants," Semi-Annual Report (Jan. 1990-June 1990) to NASA Lewis Research Center, July 1990.

27. Mueller, D.C., Scott, M.J., and Turns, S.R., "Ignition and Combustion Characteristics of Metallized Propellants," Semi-Annual Report (July 1990-Dec. 1990) to NASA Lewis Research Center, January 1991.
28. Mueller, D.C., and Turns, S.R., "Ignition and Combustion Characteristics of Metallized Propellants," Semi-Annual Report (Jan.-June 1991) to NASA Lewis Research Center, PSU Propulsion Engineering Research Center Report TR-91-008, September 1991.
29. Mueller, D.C., and Turns, S.R., "Ignition and Combustion Characteristics of Metallized Propellants," Annual Report (Aug. 1991-July 1992) to NASA Lewis Research Center, PSU Propulsion Engineering Research Center Report TR-92-010, July 1992.
30. Mueller, D.C., Scott, M.J., and Turns, S.R., "Secondary Atomization of Aluminum/RP-1 Liquid Rocket Slurry Fuels," AIAA Paper No. AIAA-91-3625, presented at the AIAA/NASA/OAI Conference on Advanced SEI Technologies, Sept. 4-6, 1991, Cleveland.
31. Mueller, D.C., and Turns, S.R., "Some Aspects of Secondary Atomization of Aluminum/Hydrocarbon Slurry Propellants," *Journal of Propulsion and Power* (submitted).
32. Wang, J.C.F., and Hencken, K.P., "In Situ Particle Size Measurements Using a Two-Color Laser Scattering Technique," *Applied Optics*, Vol. 25, 1986, pp. 653-657.
33. Brzustowski, T.A., and Glassman, I., "Vapor-Phase Diffusion Flames in the Combustion of Magnesium and Aluminum: II - Experimental Observations in an Oxygen Atmosphere," *Progress in Astronautics and Aeronautics*, Vol. 15, 1964, pp. 117-158.
34. Rautenberg, T.H., Jr., and Johnson, P.D., "Light Production in the Aluminum-Oxygen Reaction," *Journal of the Optical Society of America*, Vol. 50, 1960, pp. 602-606.
35. Krupa, R.J., Culbreth, T.F., Smith, B.W., and Winefordner, J.D., "A Flashback-Resistant Burner for Combustion Diagnostics and Analytical Spectrometry," *Applied Spectroscopy*, Vol. 40, 1986, pp. 729-733.
36. Barlow, R.S., Dibble, R.W., Chen, S.-Y., and Lucht, R.P., "Effect of Damköhler Number on Superequilibrium OH Concentration in Turbulent Nonpremixed Jet Flames," *Combust. Flame*, Vol. 82, 1990, pp. 235-251.
37. Cho, S.Y., Takahashi, F., and Dryer, F.L., "Some Theoretical Considerations on the Combustion and Disruption of Free Slurry Droplets," *Combust. Sci. and Tech.*, Vol. 67, 1989, pp. 37-57.

38. Kuo, K.K., *Principles of Combustion*, John Wiley & Sons, New York, 1986, pp. 370-385.
39. Luikov, A.V., *Heat and Mass Transfer in Capillary-porous Bodies*, Pergamon Press, Oxford, 1966.
40. Luikov, A.V., and Mikhaylov, Y.A., *Theory of Energy and Mass Transfer*, Prentice-Hall, Inc., Englewood Cliffs, 1961.
41. Reid, R.C., Prausnitz, J.M., and Poling, B.E., *The Properties of Gases and Liquids*, 4th Ed., McGraw-Hill, New York, 1987.
42. Szekely, G.A., Jr., "Experimental Evaluation of a Carbon Slurry Droplet Combustion Model," Ph.D. Thesis, The Pennsylvania State University, 1982.
43. Galecki, D.L., "Ignition and Combustion of Metallized Propellants," AIAA Paper 89-2883, July 1989.
44. Kraeutle, K.J., "Particle Size Analysis in Solid Propellant Combustion Research," *Progress in Astronautics and Aeronautics*, Vol. 53, 1977, pp. 449-463.
45. Salita, M., "Quench Bomb Investigation of  $\text{Al}_2\text{O}_3$  Formation From Solid Rocket Propellants (Part II): Analysis of Data," *25th JANNAF Combustion Meeting*, Oct. 1988, pp. 185-197.
46. Dobbins, R.A., and Strand, L.D., "A Comparison of Two Methods of Measuring Particle Size of  $\text{Al}_2\text{O}_3$  Produced by a Small Rocket Motor," *AIAA Journal*, Vol. 8, No. 9, Sept. 1970, pp. 1544-1550.
47. Parry, D.L., and Brewster, M.Q., "Optical Constants of  $\text{Al}_2\text{O}_3$  Smoke" *Journal of Thermophysics*, Vol. 5, April-June 1991, pp. 142-149.
48. Svehla, R.A., "Estimated Viscosities and Thermal Conductivities of Gases at High Temperatures," NASA Technical Report R132, 1962.
49. Konopka, W.L. Reed, R.A., and Calia, V.S., "Measurements of Infrared Optical Properties of  $\text{Al}_2\text{O}_3$  Rocket Particles," *Progress in Astronautics and Aeronautics*, Vol. 91, AIAA, New York, 1984, pp. 180-196.
50. Incropera, F.P., and DeWitt, D.P., Fundamentals of Heat and Mass Transfer - Third Edition, John Wiley and Sons, New York, 1990.
51. Siegel, R., and Howell, J.R., Thermal Radiation Heat Transfer - Second Edition, Hemisphere Publishing Corp., New York, 1981, p. 498.
52. Kofink, W., "Complete Spherical Harmonic Solution of the Boltzmann Equation for Neutron Transport in Homogeneous Media with Cylindrical Geometry," *Nucl. Sci. and Eng.*, Vol. 6, 1959, pp. 475-486.

53. White, F.M., Viscous Fluid Flow, McGraw-Hill, New York, 1974, p. 209.
54. Anon., IMSL Library Reference Manual, IMSL, Inc., January 1, 1982.



## APPENDIX - PUBLICATIONS AND PRESENTATIONS

Mueller, D.C., Scott, M.J., and Turns, S.R., "Secondary Atomization of Aluminum/RP-1 Liquid Rocket Slurry Fuels," AIAA Paper No. AIAA-91-3625, presented at the AIAA/NASA/OAI Conference of Advanced SEI Technologies, Sept. 4-6, 1991, Cleveland.

Mueller, D.C., and Turns, S.R., "Some Aspects of Secondary Atomization of Aluminum/Hydrocarbon Slurry Propellants," *Journal of Propulsion and Power* (submitted).

Turns, S.R., "Ignition and Combustion of Aluminum Slurry Propellants," Penn State Propulsion Engineering Center, 1st Annual Symposium at the 25th Joint Propulsion Conference, July 10-13, 1989, Monterey, CA.

Turns, S.R., "Ignition and Combustion of Metallized Propellants," presented at the Penn State Propulsion Engineering Center 2nd Annual Symposium at the NASA Space Transportation Propulsion Technology Symposium, June 25-29, 1990, University Park, PA.

Turns, S.R., Mueller, D.C., and Scott, M.J., "Secondary Atomization of Aluminum/RP-1 Liquid Rocket Slurry Fuels," presented at the Fall Technical Meeting 1990, Eastern Section: The Combustion Institute, December 3-5, 1990, Orlando, FL.

Mueller, D.C., and Turns, S.R., "Aluminized Propellants for Liquid Rockets: Effects of Secondary Atomization on Performance," presented at the Penn State Propulsion Engineering Research Center 4th Annual Symposium, Sept. 9-10, 1992, Marshall Space Flight Center, Huntsville, AL.

